Received: 28 November 2024 | Revised: 14 October 2025 | Accepted: 2 December 2025

DOI: 10.33012/navi.754

ORIGINAL ARTICLE

Real-Time Ionospheric Threat Adaptation to Increase CAT-I GBAS Availability in Equatorial Regions

Maria Caamano*[1,2] | Jose Miguel Juan[2] | Jaume Sanz[2] | Sam Pullen[3]

[1] Institute of Communications and Navigation, German Aerospace Center (DLR), Wessling, Germany

[2] Research group of Astronomy and Geomatics (gAGE), Universitat Politècnica de Catalunya (UPC), Barcelona, Spain

[3] Dept. of Aeronautics and Astronautics, Stanford University, California, United States of America

Correspondence
*Maria Caamano
Institute of Communications and Navigation, German Aerospace Center (DLR), Wessling, 82234, Germany.
Email: maria.caamanoalbuerne@dlr.de

Abstract

Current solutions to mitigate errors caused by undetected anomalous ionospheric gradients in ground-based augmentation systems (GBASs) rely on conservative threat models. While effective, these models limit system availability, particularly in regions with highly active ionospheric conditions.

In this paper, we propose a methodology to replace the worst-case large values of existing conservative threat models with the magnitudes of real-time observed anomalous ionospheric gradients. This approach involves determining the maximum anomalous ionospheric gradients that could be affecting a specific GBAS station without being detected by a network of dual-frequency global navigation satellite system monitoring stations protecting it.

Using simulations and real data from a monitoring network in Brazil, we demonstrate that this methodology significantly enhances category-I GBAS availability in regions with active ionospheric conditions. Moreover, the proposed approach is compatible with current algorithms and hardware, enabling its adaptation for certification when tailored to the specific characteristics of a given region.

Keywords

anomalous ionospheric gradients, availability, ground-based augmentation system (GBAS), real-time integrity monitoring

1 | INTRODUCTION

For more than 50 years, airports have relied on instrument landing systems (ILSs) to provide pilots with approach and landing guidance in low-visibility conditions. Although these systems have proved to be reliable and functional, ILSs are costly to maintain and have operational limitations that reduce runway capacity. In contrast to the conventional ILSs in use today, a ground-based augmentation system (GBAS) station can provide approach guidance to multiple runway ends at an airport and can thus significantly reduce the required amount of infrastructure and associated costs.

A GBAS station transmits differential corrections and integrity parameters to airborne users. The differential corrections allow airborne users to correct most of the spatially correlated global navigation satellite system (GNSS) ranging errors and thus improve the accuracy of their position estimations. The nominal residual

errors that remain are bounded by so-called protection levels (PLs), which are computed with the transmitted integrity parameters and airborne models. The PLs are compared to the alert limits (ALs), the maximum allowable error bounds. If any of the PLs exceed the corresponding ALs, the aircraft considers the output of the multi-mode receiver as unavailable for guidance and therefore will not use the GBAS for precision approach and landing.

However, under abnormal ionospheric activity such as large ionospheric gradients, there could be a large difference between the ionospheric error experienced by the GBAS reference station and the aircraft on approach. Because this error is not corrected through the use of differential corrections and is also not overbounded by the PLs, the presence of spatial abnormal ionospheric gradients may lead to non-differentially-corrected and insufficiently bounded position errors (Pullen et al., 2009). The protection of airborne users against the ionospheric gradient threat has already been tackled in the current GBAS approach service types (GAST) C and D, which are based on the L1 Global Positioning System (GPS) signals.

In GAST C, it is the sole responsibility of the ground subsystem to ensure mitigation of anomalous ionospheric errors. GAST C currently supports category-I (CAT-I) operations and has recently been demonstrated to enable category-II (CAT-II) operations at Frankfurt Airport. GAST C could potentially support CAT-II operations in other airports as well in the future, particularly in regions with typically calm ionospheric conditions, such as certain mid-latitude areas. The GAST C station operates a code carrier divergence (CCD) monitor that allows the detection of ionospheric anomalies (Simili & Pervan, 2006). However, this monitor alone is not sufficient to mitigate all hazardous ionospheric errors. For this reason, a GAST C ground station verifies by simulation that each satellite geometry potentially usable at the aircraft (PLs $\leq$ ALs) is safe in the presence of an ionosphere-anomaly threat applicable in the region through a process called "position-domain geometry screening" (PDGS) (Lee et al., 2011; Seo et al., 2012; Yoon et al., 2019). In the case that a simulated satellite geometry is not safe, the ground station inflates the integrity parameters so that the PLs exceed the ALs when an arriving aircraft aims to use this satellite geometry, notifying the aircraft that the GBAS should not be used for guidance. These ionosphere-anomaly threats form the so-called "ionospheric threat model," which is based on the worst-ever-experienced ionospheric gradients measured in the relevant regions and defines a range of values for gradient parameters that could harm the GBAS (Datta-Barua et al., 2010; Mayer et al., 2009; Saito et al., 2017; Yoon et al., 2017). Figure 1 shows the typical ionospheric threat model used in mid-latitude and high-latitude regions, the so-called wedge model, together with its parameters: the slant slope of the gradient (g_{iono}) in mm/km, which describes

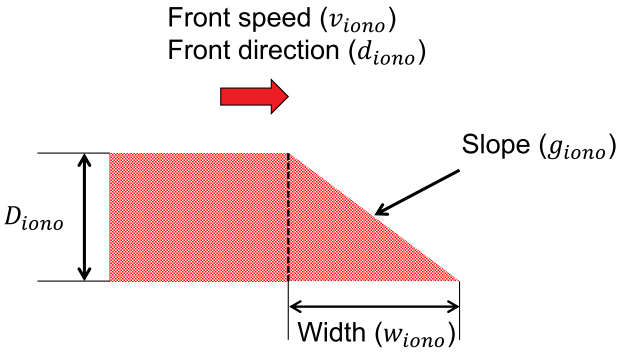

FIGURE 1 GBAS ionospheric threat model

the decorrelation of the ionosphere with distance, the maximum ionospheric delay (D_{iono}) in meters, the width of the gradient (w_{iono}) in km, and the speed (v_{iono}) in m/s and direction (d_{iono}) in degrees of the gradient.

The main challenge of PDGS is that it assumes that the "worst-case" or largest gradient is always present, which is a highly conservative assumption. This assumption, together with the high values of the threat model in equatorial regions (Saito et al., 2017; Yoon et al., 2017), which are caused by so-called equatorial plasma bubbles (EPBs), leads to a limited availability of CAT-I GBAS (approximately 58.3% in Rio de Janeiro, Brazil) that is far below the requirements (Yoon et al., 2019).

Therefore, recent studies have focused on reducing the above conservative assumptions in order to meet CAT-I availability requirements in equatorial regions. Yoon et al. (2019) proposed a probabilistic method that uses Monte Carlo simulations and a prior probability of the occurrence of extreme EPBs to reduce the required inflation factors. However, although the system availability for CAT-I precision approaches improved to 89.6% in Rio de Janeiro, it is not yet sufficient to achieve the required availability of 99%. Yoon et al. (2020) proposed to use existing information about the characteristics of EPBs to improve the stochastic approach developed by Yoon et al. (2019). However, the lack of sufficient historical data collected during large ionospheric events in equatorial regions might limit the use of this approach. Furthermore, this method cannot predict or protect against a larger gradient that might occur at some time point in the future.

In GAST D, new monitors implemented on the aircraft and ground are responsible to mitigate these errors and their risks (Pullen et al., 2017). However, owing to the observed sensitivity of the proposed monitors to the characteristics of the ionosphere in equatorial regions, it is expected that the current version of GAST D will not meet the operational requirements (especially continuity and availability) in regions with more severe ionospheric conditions than those present in mid-latitudes (International Civil Aviation Organization, 2017). Therefore, over the last years, the prime focus has been to achieve the required level of availability and continuity for GAST C stations in equatorial regions.

All of the methodologies mentioned above for ionospheric threat mitigation in GBASs have one characteristic in common: they consider only the ionospheric information obtained from ground infrastructure installed inside the protected area of the airport or from the aircraft itself. This situation implies poor observability of certain gradients and forces the GBAS ground station to make conservative assumptions to protect integrity, which impacts the availability of the system.

To address this issue, Lee et al. (2016) proposed a real-time ionospheric threat adaptation methodology that incorporates predicted values of space weather indices. However, space weather prediction is inherently unreliable because of prediction errors; to account for this unreliability, the authors also developed an uncertainty model derived from historical data. This model helps to incorporate external space weather data into the GBAS. Despite the potential benefits of this approach, it also introduces risks: these space weather indices are sourced from external entities, which could lead to both integrity and security issues. Moreover, the methodology by Lee et al. (2016) was only tested with data from mid-latitudes, where ionospheric activity is generally less intense compared with equatorial regions, limiting its applicability to more active environments.

In contrast, Marini-Pereira et al. (2024) proposed a different approach, assuming a constant ionospheric gradient of 400 mm/km and discarding satellites that exceed a specified alert threshold. This threshold was specifically designed to detect gradients above 400 mm/km, ensuring that, when combined with PDGS, the system would meet the availability and continuity requirements for CAT-I GBAS

operations. However, their method does not account for the direction of gradient propagation or correct for the movement of the ionospheric pierce points (IPPs) relative to the gradient. The IPPs refer to the intersections between the satellite–ground receiver line of sight and the ionosphere, which is modeled as a thin shell layer located 350 km above the Earth's surface. This limitation means that anomalous gradients could go undetected or be underestimated, particularly if the IPPs are moving toward a gradient at an angle other than the direction of propagation. Thus, it may be overly optimistic to assume that all gradients greater than 400 mm/km are detected. Additionally, the required detection time for anomalous gradients could extend up to 20 min, which may not meet the stringent time-to-alert requirements of GBASs.

In previous work (Caamano et al., 2021), we proposed a real-time ionospheric monitoring approach based on a network of dual-frequency monitoring stations (external to the GBAS installation) that could reduce the conservative assumptions currently applied in GAST C and GAST D. We described algorithms for detecting anomalous ionospheric gradients and estimating the gradient parameters and evaluated our algorithms with simulated and real data representative of the region of Alaska. In a follow-up article (Caamano et al., 2025), we adapted this methodology to work in the equatorial region and proposed a method for overbounding the estimated gradient parameters to meet GBAS requirements.

In this paper, we propose a methodology to integrate the information provided by the real-time monitoring network into a GAST C station. Based on the performance of the network in detecting and estimating gradients, the algorithm proposed in this study adjusts the threat model values that act as input to the PDGS. Therefore, the proposed method is compatible with existing algorithms and hardware. After describing the methodology, we assess the availability of a GAST C station based on the performance of a real network of stations located in Brazil. Additionally, we conduct a comparative analysis, contrasting the computed availability of a GAST C station with network support against the hypothetical availability of the same GAST C station without such network support in the same geographical location. This approach shows the impact of real-time monitoring on current conservative GBAS threat models and presents practical implications for the performance and availability of GAST C stations.

This paper is organized as follows: Section 2 briefly describes the calculation of PLs and the PDGS algorithm. Section 3 describes the functioning of the network and the methodology used to derive the minimum detectable gradient (MDG) via this network. Section 4 introduces the data used for our evaluations, and Section 5 introduces the simulation setup. Finally, Section 6 presents the availability results obtained by using the proposed methodology for a calm day and two active days.

2 | BACKGROUND

2.1 | PL Calculation

The PLs are defined as position error bounds at the defined integrity risk probabilities ($2 \cdot 10^{-7}$ per approach) (International Civil Aviation Organization, 2017). They address the fault-free condition (H0), the case of a failure in one of the reference receivers (H1), and the position errors due to errors in the ephemeris data. The aircraft computes the maximum among the three PLs and verifies whether the values are below the lateral and vertical ALs (LAL and VAL, respectively). Because the vertical PL (VPL) is usually larger than the lateral PL (LPL) whereas the VAL is

smaller than the LAL, our assessments are based on the VPL and the VAL. The VPL in fault-free conditions (VPL_{H0}) is calculated at each epoch using Equation (1):

$$VPL_{H0} = k_{ffmd} \cdot \sqrt{\sum_{j=1}^{J} (s^j_{apr\_vert})^2 \cdot (\sigma^j_{GBAS})^2} \tag{1}$$

where index j indicates the j-th satellite of the J satellites used for the VPL computation, σ^j_{GBAS} is the standard deviation of a normal distribution that bounds the true post-correction range-domain error distribution for satellite j under the fault-free hypothesis, and k_{ffmd} is the fault-free missed detection multiplier. The components of σ^j_{GBAS} are as follows:

$$\sigma^j_{GBAS} = \sqrt{(\sigma^j_{pr\_gnd})^2 + (\sigma^j_{tropo})^2 + (\sigma^j_{pr\_air})^2 + (\sigma^j_{iono})^2} \tag{2}$$

where $\sigma^j_{pr\_gnd}$ is the total fault-free standard deviation of the error contained in the differential corrections for satellite j, σ^j_{tropo} is the standard deviation of the error term associated with residual tropospheric uncertainty for satellite j, $\sigma^j_{pr\_air}$ is the corresponding error term that bounds fault-free airborne receiver multipath and noise errors for satellite j, and σ^j_{iono} accounts for the nominal residual ionospheric uncertainty for satellite j. The $s^j_{apr\_vert}$ values are calculated as follows:

$$s^j_{apr\_vert} = s_{3j} + s_{1j} \cdot \tan(\theta_{GPA}) \tag{3}$$

where θ_{GPA} is the glide path angle (typically 3°) and s_{1j} and s_{3j} correspond to the first and the third rows and column j of the pseudoinverse $\mathbf{S}$ of the weighted geometry matrix $\mathbf{G}$ containing all of the available satellites, which can be written as follows:

$$\mathbf{S} = (\mathbf{G}^T\mathbf{W}\mathbf{G})^{-1}\mathbf{G}^T\mathbf{W} \tag{4}$$

Each row of $\mathbf{G}$ is defined as follows:

$$[-\cos(\theta^j)\cdot\cos(\psi^j), -\cos(\theta^j)\cdot\sin(\psi^j), -\sin(\theta^j), 1] \tag{5}$$

with θ^j and ψ^j being the elevation and azimuth of the j-th satellite, respectively. The inverse of the weighting matrix is defined as follows:

$$\mathbf{W}^{-1} = \begin{pmatrix} (\sigma^j_{GBAS})^2 & \cdots & 0 \\ \vdots & \ddots & \vdots \\ 0 & \cdots & (\sigma^J_{GBAS})^2 \end{pmatrix} \tag{6}$$

Additionally, the vertical ephemeris PL (VPB) is defined as follows:

$$\begin{aligned} VPB^j &= \left|s^j_{apr\_vert}\right| \cdot x_{air} \cdot P^j + k_{md\_e} \cdot \sqrt{\sum_{j=1}^{J} (s^j_{apr\_vert})^2 \cdot (\sigma^j_{GBAS})^2} \\ VPB &= \max\left(VPB^j\right) \end{aligned} \tag{7}$$

where x_{air} is the distance (in slant range) between the aircraft and the GBAS reference point (in meters), k_{md_e} represents the ephemeris missed detection

multiplier, and P^j represents the ephemeris decorrelation parameter for satellite j. The last two parameters are both dependent on the approach service type (see Section 2.3.11.5.2.4 of RTCA (2017)). In this work, we use both VPL_{H0} and VPB, as these terms are the most relevant when studying availability. Therefore, VPL_{H1} is considered to be beyond the scope of this work.

2.2 | Position-Domain Geometry Screening

This section gives a brief summary of the PDGS algorithm, which is then applied in the following sections. More detailed information can be found in works by Lee et al. (2011), Ramakrishnan et al. (2008), Seo et al. (2012), and Yoon et al. (2019).

The PDGS algorithm primarily consists of three parts: (i) simulation of the worst-case ionosphere-induced range errors based on the established ionospheric threat model, (ii) computation of the maximum vertical ionosphere-induced position errors (MIEVs), and (iii) inflation of the broadcast integrity parameters.

2.2.1 | Ionosphere-Induced Range Error Simulation

The ionosphere-induced range error simulation determines the worst-case differential ionosphere-induced range errors that could occur in the aircraft in the presence of an ionospheric anomaly. Kim et al. (2021) derived closed-form expressions from exhaustive simulations considering the Brazilian threat model and the detectability of the CCD monitor. The formulas presented by Kim et al. (2021) are used in this work to calculate the ionosphere-induced range error (ε) for the PDGS, as summarized in the following.

Case 1: Very small relative speed of the ionospheric front and IPP

When the relative speed of the ionospheric front and IPP (Δv) is close to zero, the CCD monitor cannot detect anomalous ionospheric gradients. In this case, the ionosphere-induced differential range error, ε, is calculated in meters using Equation (8):

$$\varepsilon = \min\left(\frac{D_{iono}}{w_{iono}}, g_{iono}\right)\cdot\left(x_{Air} + 2\cdot\tau\cdot v_{Air}\right), \quad \text{if} \quad \Delta v \le a \tag{8}$$

with:

$$a = \frac{MDDR_{ccd}}{2\cdot\min\left(\frac{D_{iono}}{w_{iono}}, g_{iono}\right)} \tag{9}$$

Here, $MDDR_{ccd}$ is the minimum detectable divergence rate of the CCD monitor, D_{iono} is the maximum ionospheric delay considered in the threat model (in meters), w_{iono} is the ionospheric front width (kilometers), g_{iono} is the ionospheric gradient (m/km), x_{Air} is the physical separation between the GBAS ground facility and an approaching airplane (kilometers), τ is the time constant of the single-frequency GBAS carrier-smoothing filter, which is 100 s for CAT-I GBAS, v_{Air} is the velocity of the aircraft on approach (km/s), and a is the relative speed Δv at which the CCD monitor begins to detect the anomalous ionospheric gradient.

Case 2: Moderate relative speed of the ionospheric front and IPP

In this case, the CCD monitor begins to detect anomalous ionospheric gradients, and the ionosphere-induced differential range errors are calculated as in Equation (10):

$$\varepsilon = \frac{2 \cdot \tau \cdot v_{Air} \cdot g_{iono}}{a - b} \cdot (\Delta v - b) + g_{iono} \cdot x_{Air}, \quad \text{if} \quad a < \Delta v \leq b \tag{10}$$

where b is the Δv value at which the differential range error calculated from the exhaustive simulations is at a minimum (see Figure 10 of Kim et al. (2021)), calculated as follows:

$$b = \frac{0.0165}{g_{iono}} + 0.113 \tag{11}$$

Case 3: Large relative speed of the ionospheric front and IPP

In this case, the CCD monitor alerts with a very small probability of missed detection, and the potential ionosphere-induced differential errors do not grow over the value calculated from Equation (12):

$$\varepsilon = g_{iono} \cdot x_{\text{Air}}, \quad \text{if} \quad \Delta v > b \tag{12}$$

2.2.2 | Maximum Ionospheric Vertical Position Errors

The previous step provides the ionosphere-induced range error per satellite. Based on this output, ionosphere-induced position errors can be computed by considering potential satellite geometries. For this purpose, first, the GBAS ground station generates all possible subsets of geometries from an all-in-view set of J usable satellites down to $J-2$. This step assumes that the aircraft might not use up to two satellites from the satellites visible to and approved by the ground station because of, e.g., maneuvering, filter convergence, etc.

Then, the ionosphere-induced vertical position errors (IEVs) are computed for each subset satellite geometry, with the assumption that two satellites are simultaneously affected by the ionospheric front, as in the works by Lee et al. (2011) and Seo et al. (2012). In this case, the so-called two-affected-satellites scenario, it is also assumed that the IPP velocity of one satellite projected onto the direction of propagation of the ionospheric front is approximately the same as the velocity of the ionospheric front. Consequently, the relative velocity between the front and the first satellite is considered to be approximately zero.

Because the worst possible satellite pair in terms of position error cannot be predicted *a priori*, all possible independent satellite pairs (j_1, j_2) must be considered for each subset geometry. Once all possible satellite subsets have been identified, the IEV for each of these subsets and each pair of satellites (j_1, j_2) is calculated as follows:

$$\begin{aligned} IEV^{j_1,j_2} = \max\Bigg\{ & \left| s^{j_1}_{apr\_vert} \cdot \varepsilon^{j_1} + s^{j_2}_{apr\_vert} \cdot \varepsilon^{j_2} \right|, \left| s^{j_1}_{apr\_vert} \cdot \varepsilon^{j_1} - \gamma \cdot s^{j_2}_{apr\_vert} \cdot \varepsilon^{j_2} \right|, \\ & \left| s^{j_2}_{apr\_vert} \cdot \varepsilon^{j_2} - \gamma \cdot s^{j_1}_{apr\_vert} \cdot \varepsilon^{j_1} \right| \Bigg\} \end{aligned} \tag{13}$$

where s_{apr_vert} is the vertical position component of the weighted-least-squares projection matrix $\mathbf{S}$ for satellite j_1 or j_2 (see Equation (3)), ε is the ionosphere-induced range error for satellite j_1 or j_2, and γ is a dimensionless constant between 0 and 1 used to overbound the errors introduced by any observed ionosphere anomaly. When γ is equal to 1, the IEV reaches its most conservative value (Seo et al., 2012).

The IEVs for both satellites are computed, and the largest IEV is selected as the value of that satellite pair. After the IEV has been computed for all satellite pairs from a subset geometry, the MIEV for this subset is calculated as the maximum of the IEVs.

The previously described methodology can be applied to all regions in the world. However, in Brazil, where the threat model specifies certain limits for the direction of EPB propagation, the selection of satellite pairs for the two-affected-satellites scenario is specified within the orientation angle constraint given by the limit on the EPB tilt angle (Yoon et al., 2019). In this work, we have implemented this methodology as described by Yoon et al. (2019).

The MIEV for each satellite subset that might be utilized by the airborne user is compared with the CAT-I tolerable error limit (TEL) in the vertical direction, which is 28.78 m at the minimum decision height (DH) of 200 feet (Shively & Niles, 2008). If the MIEV of a subset exceeds the TEL, this particular satellite geometry must be excluded in order to mitigate the potential integrity risk. The geometry is excluded by inflating the broadcast integrity parameters.

2.2.3 | *Inflation of Integrity Parameters*

The goal of this step is to inflate the broadcast integrity parameters such that the potentially hazardous satellite geometries that generate MIEVs exceeding the TEL are excluded. The reason for this is that when the ground station inflates the integrity parameters, the VPLs computed in the aircraft increase accordingly.

Therefore, several possibilities have been studied in the literature for inflation of the integrity parameters: σ_{vig} inflation, which inflates the part of σ_{iono} that describes the nominal vertical ionospheric decorrelation between the GBAS station and the user (Lee et al., 2011; Lee et al., 2006; Seo et al., 2012; Yoon et al., 2019), and σ_{pr_gnd} and P-value inflation (Lee et al., 2006; Ramakrishnan et al., 2008; Seo et al., 2012; Yoon et al., 2019). From these possibilities, σ_{vig} inflation is the most commonly used method. However, several studies (Yoon et al., 2019; Yoon et al., 2016) in which the geometry screening algorithm has been applied together with the Brazilian threat model have suggested that when this threat model is utilized, σ_{vig} can occasionally reach the maximum value that can be transmitted in the GBAS messages. Therefore, in this case, the σ_{vig} parameter is inflated until it reaches a maximum value of 25.5 mm/km; then, σ_{pr_gnd} is inflated as needed until all potential hazardous satellite geometries are screened out. Silva and Monico (2022) also studied the relationship between the σ_{vig} value and GBAS CAT-I availability in Brazil.

3 | METHODOLOGY

3.1 | The Network–GBAS Concept

In previous work (Caamano et al., 2021), we proposed a methodology for detecting and estimating anomalous ionospheric gradients using a wide area network

of dual-frequency GNSS stations, external to the GBAS installation, situated in carefully surveyed locations. In this section, we summarize the functionality of the proposed monitoring network and describe how the network's information can be included in the current GBAS algorithms to mitigate the ionospheric gradient threat.

First, the processing component for each station in the network receives GNSS dual-frequency code- and carrier-phase measurements and calculates the geometry-free combination of the carrier-phase measurements at the current epoch t, as in Equation (14) (Equation (5.33) of the work by Misra and Enge (2006)):

$$\hat{I}^{j}_{f_1,r}(t) = \frac{(f_2)^2}{(f_1)^2 - (f_2)^2} \cdot \left(\phi^{j}_{f_1,r}(t) - \phi^{j}_{f_2,r}(t) \right) \tag{14}$$

where $\phi^{j}_{f_1,r}(t)$ is the carrier-phase measurement in meters for frequency f_1 (e.g., L1/E1) and $\phi^{j}_{f_2,r}(t)$ is the carrier-phase measurement in meters for frequency f_2 (e.g., L5/E5a). The station that calculates the geometry-free combination is r, which is identified by a certain station name and belongs to the set of the monitoring network of stations denoted as $\mathcal{R}$. Note that the result of Equation (14) can be considered as an estimate of the slant ionospheric delay with errors (e.g., carrier-phase ambiguities). Because this work considers only the slant ionospheric delay calculated for the L1/E1 frequency, frequency subscripts are omitted in the following.

The test statistics of the monitoring network are the rates of change of the estimated ionospheric delays corresponding to each satellite j and each station r, computed as follows:

$$Itest^{j}_{r}(t) = \frac{\hat{I}^{j}_{r}(t) - \hat{I}^{j}_{r}(t-1)}{\Delta T} \tag{15}$$

Here, $\hat{I}^{j}_{r}(t)$ is the slant ionospheric delay estimation calculated from Equation (14) for station r, satellite j, and epoch t, $\hat{I}^{j}_{r}(t-1)$ is the slant ionospheric delay estimation for station r, satellite j, and the previous epoch, and ΔT is the time difference between two consecutive epochs. Note that when the test statistics are computed as the first derivative of the ionospheric delays based on Equation (14), the errors mentioned above cancel out because they are constant over time.

The test statistics are compared with predefined thresholds derived from real measurements collected in nominal conditions (i.e., without anomalous ionospheric gradients) from each of the stations r and integrity requirements. These thresholds indicate whether there is a significant perturbation affecting each of the satellite–station pairs in real time. Given an acceptable false alert probability, P_{fa}, a threshold for each station can be defined as follows:

$$Thr_r(\theta_m) = \mu_{Itest_r}(\theta_m) \pm k_{fa} \cdot I_{monitor,r}(\theta_m) \cdot \sigma_{Itest_r}(\theta_m) \tag{16}$$

where $\sigma_{Itest_r}(\theta_m)$ is the standard deviation of the $Itest_r(\theta_m)$ distribution composed of the $Itest^{j}_{r}(t)$ samples for all satellites and epochs arranged into elevation bins, with θ_m and $m = 1, 2, .., \mathcal{M}$ representing the elevation bins. Moreover, $\mu_{Itest_r}(\theta_m)$ is the mean of the $Itest^{j}_{r}(t)$ distribution computed in each elevation bin, $I_{monitor,r}(\theta_m)$ is the inflation factor calculated to overbound the tails of the distribution per elevation bin, and k_{fa} is the false alert multiplier computed from the inverse of the standard normal cumulative distribution, $Q^{-1}\left(\frac{P_{fa}}{2}\right)$. More details

about the threshold derivation with real data from two station networks in Alaska and Brazil have been reported by Caamano et al. (2021, 2025).

The detection information from each station observing a given satellite is shared within the network in real time. For the case in which several monitoring stations have detected the same ionospheric gradient, a central processor estimates and overbounds its parameters, by considering a previously derived uncertainty model (Caamano et al., 2021, 2025).

Each GBAS station would be then responsible for using the network information to adjust the integrity parameters and support the already existing equipment in covering the GBAS approaches at each airport. Specifically, we propose a methodology that incorporates this information in a GAST C station via the PDGS algorithm. In this way, a GAST C ground station would use a variable maximum gradient slope per satellite, g_{iono}^{j}, in the calculation of anomalous ionosphere-induced differential range errors within the PDGS algorithm (in Equations (8)–(12) from Section 2) instead of using the constant value from the threat model, as is currently done. This variable maximum gradient slope takes one of the following values, depending on the information received from the network:

(i) The MDG or largest gradient that could be affecting the supported GBAS stations without being detected by the network. This value would be used as the maximum anomalous gradient that can currently occur when the network does not detect any anomalous activity.
(ii) The "maximum possible slope" estimated and overbounded in real time for each satellite in the coverage area of the network, when the network detects an anomalous ionospheric gradient and the estimation algorithms converge.
(iii) A "warning" that implies the use of the "worst-case" ionospheric threat model applicable to the GBAS for that area, when the network detects an anomalous ionospheric gradient but the algorithms are not yet able to reliably estimate the gradient parameters. The "worst-case" ionospheric threat model would also be used in two additional cases: in the case that the "maximum possible slope" from point (ii) exceeds its "worst-case" bounds, as it has much less statistical uncertainty than the real-time gradient estimates, and in the case that the signal is lost at several stations, indicating the presence of severe scintillation.

Therefore, the integrity parameters transmitted by the GAST C station using the proposed method would require less inflation most of the time. Thus, availability would increase in regions where conservative ionospheric threat models must be applied to protect integrity. Results justifying the previous statements are presented in Section 6. Figure 2 shows a diagram of the interface between the GBAS and the network.

3.2 | Derivation of the MDG by the Network

The detection threshold derived for each monitoring station considers a certain probability of false alert, but these thresholds do not consider any probability of missed detection. However, because the goal of this work is to substitute the current conservative threat model for the output of the network, the network itself must cover the integrity budget allocated to the threat model. Although the ionospheric threat model is considered to always be true and, in principle, it does not

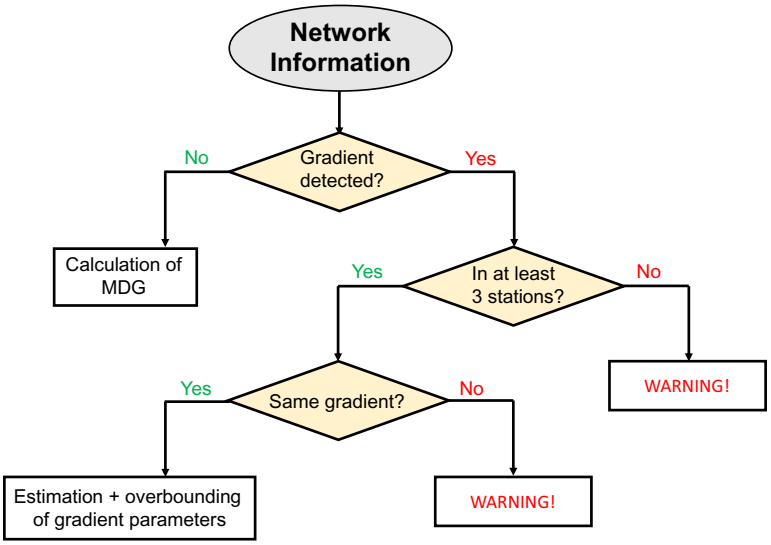

FIGURE 2 Flow chart of the network decision logic

have a fixed integrity budget associated with it, in Section D.3 of Eurocae (2013) ("GBAS integrity risk not covered by protection levels"), it is stated that *"The GBAS Ground Subsystem integrity risk is less than* $1.5 \cdot 10^{-7}$ *in any one approach. [...] The integrity risk due to Ground Subsystem failures can be divided into risks associated with undetected events of environmental anomalies (Note 1) and Ground Subsystem failures resulting in erroneous GBAS messages. [...] Anomalous ionosphere, anomalous troposphere, excessive radio-frequency interference (RFI) and excessive multipath are notably considered as environmental anomalies."* This description corresponds to the probability of loss of integrity (LOI) allocated to faults different from individual satellite failures not bounded by any PLs, which is $1 \cdot 10^{-8}$ in Figure 2 of Pullen and Enge (2007). A part of this integrity budget should be sub-allocated to anomalous ionosphere. The GBAS manufacturer selects these allocations according to the characteristics of the GBAS station (e.g., detectability of the implemented monitors). As a simplification, this work considers a sub-allocated probability of LOI per 150-s approach for abnormal ionospheric activity ($P_{LOI,abnormal\_iono}$) of $1 \cdot 10^{-8}$ from the total of $1.5 \cdot 10^{-7}$ (integrity risk allocation for H2 conditions in Figure 2 of Pullen and Enge (2007)), as in the work by Yoon et al. (2019). Sub-allocations for other anomalous conditions, such as anomalous troposphere, have not been considered. Therefore, the following condition must be fulfilled (Yoon et al., 2019):

$$P_{LOI,abnormal\_iono} \geq P_{md,abnormal\_iono} \cdot P_{prior,abnormal\_iono} \tag{17}$$

where $P_{md,abnormal\_iono}$ is the probability of missed detection given the existence of abnormal ionospheric activity and $P_{prior,abnormal\_iono}$ is the prior probability of an anomalous ionospheric gradient occurring. Typically, $P_{prior,abnormal\_iono}$ is assumed to be 1 and $P_{md,abnormal\_iono} = P_{LOI,abnormal\_iono}$, but recent studies have also assumed this prior probability to be $P_{prior,abnormal\_iono} = 10^{-3}$ (Yoon et al., 2020; Yoon et al., 2019).

Furthermore, the amount that each network station must cover from this integrity budget depends on the characteristics of the ionospheric gradients in the specific region, the number of stations composing the network, and the location of the GBAS station(s) within the protected area of the network. In the following, several

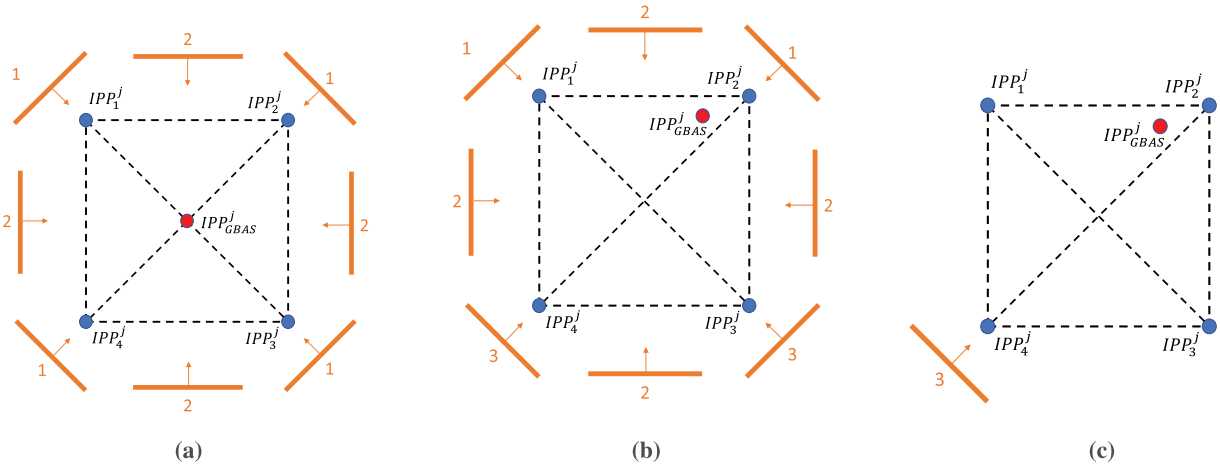

FIGURE 3 Example of a square-shaped network, where the GBAS station to be protected is located in different positions within the station network. (a) GBAS station located in the center of the network and an ionospheric front moving in all directions. (b) GBAS station located near the side of the network and an ionospheric front moving in all directions. (c) GBAS station located near the side of the network and an ionospheric front moving from southwest to northeast.
The four blue circles represent four IPPs belonging to the same satellite and four different stations, and the red circle represents the IPP belonging to the same satellite and the GBAS station. In Figures 3(a)–3(c), the orange lines represent the gradient fronts moving toward the IPPs from different directions, and the numbers near each front represent the number of stations that might detect the ionospheric front before it arrives at the IPP belonging to the GBAS station.

examples are presented for calculating the $P_{md,abnormal\_iono}$ that each monitoring station would need to cover, conservatively assuming $P_{prior,abnormal\_iono} = 1$. Note that once the network is operational, it could compute $P_{prior,abnormal\_iono}$ based on the data it processes.

Figure 3(a) shows an example of a square-shaped network configuration, where the single-protected GBAS station is located in the center. Here, the four blue circles represent four IPPs belonging to the same satellite and four different stations, and the red circle represents the IPP belonging to the same satellite and the GBAS station. Note that this is a simplification, as the geometry of the stations on the ground can be considered similar to that of the IPPs only when the satellites are at medium or high elevations (Hernández-Pajares et al., 2006). Assuming that the probability of a gradient moving in any direction is typically the same, the most representative directions for a gradient moving toward the network are represented as arrows perpendicular to the ionospheric front. As shown in Figure 3(a), a gradient moving from north to south could be detected by two stations before the gradient impacts the IPP of the GBAS station. This situation is represented by a "2" written above this direction. However, a gradient moving from northeast to southwest could only be detected by one station before it impacts the GBAS, because the other two stations are aligned with the gradient. This situation is represented by a "1" written above this direction. This process is repeated for all directions of the gradient.

Then, for each direction, the probability of missed detection for each station is calculated, assuming that they are statistically independent. For example, when a gradient arrives from north to south, the two top stations would each need to cover a $P_{md,abnormal\_iono}$ of 1×10^{-4} and the two bottom stations are not considered, as they are located after the GBAS station. For a gradient moving from northeast to southwest, only one station can detect the gradient; therefore, that station would

need to assume the whole budget of 1×10^{-8}, while the other stations are not considered. Once this study has been performed for all possible directions, the "worst case" for each station is selected, which corresponds to the lowest $P_{md,abnormal\_iono}$. The "worst case" for all corners in Figure 3(a) is that only one station can detect the gradient and, therefore, all corners need to cover a $P_{md,abnormal\_iono}$ of 1×10^{-8}.

However, the situation changes if the GBAS station is not situated in the center of the square, as depicted in Figure 3(b). Here, only the two stations located in the upper part of the square have to cover the total integrity budget, 1×10^{-8}, while the stations located in the lower part of the square only have to cover 1×10^{-4}. Considering that most networks will have more stations available in more complex configurations, the $P_{md,abnormal\_iono}$ that will need to be covered by each station will likely be less restrictive.

Furthermore, there exist ionospheric threat models that do not consider all directions of the ionospheric gradient, e.g., the threat model in Brazil (Yoon et al., 2017). This case is exemplified in Figure 3(c) with a single direction representing the very limited range of directions that must be considered. Here, the integrity budget is distributed among all stations that could be impacted before the gradient reaches the GBAS, but only one direction is considered. This differs from the previous examples in that there is no "worst case" for the remaining corners that is more conservative, and therefore, the integrity budget can be distributed equally among these stations.

At this point of the methodology, we assume that satellites exhibit similar behavior in terms of the geometry defined by their IPPs computed with the different reference stations and the GBAS. For instance, a high-elevation satellite will generally present an IPP geometry similar to that of the locations of all stations (1–4) and the GBAS on the ground, because its signal paths intersect the ionosphere nearly vertically, minimizing variation. In contrast, a low-elevation satellite will produce a more distorted IPP geometry that does not resemble the locations of the GBAS and the network reference stations on the ground. Therefore, this initial computation should ideally account for all possible satellite elevations and the corresponding IPP geometries for each satellite, each reference station in the network, and the GBAS. While this approach would provide a more accurate representation, it would also significantly increase the complexity. However, this is only a preliminary calculation; all potential geometries are later comprehensively considered in the Monte Carlo simulations (explained in Section 5) during the MDG computation. Therefore, this simplification does not affect the validity of the results.

Following this step, the $P_{md,abnormal\_iono,r}$ for each network station can be computed only once. Next, the minimum detectable error (MDE) is calculated for each of the stations composing the network. The MDE has the same units as the threshold, mm/s in this case, and is computed as follows:

$$MDE_r(\theta_m) = Thr_r(\theta_m) + k_{md,abnormal\_iono,r} \cdot I_{monitor,r}(\theta_m) \cdot \sigma_{Itest_r}(\theta_m) \tag{18}$$

where $k_{md,abnormal\_iono,r}$ is the scalar multiplier needed to meet the required $P_{md,abnormal\_iono,r}$ previously calculated and computed from the inverse of the standard normal cumulative distribution, $Q^{-1}(P_{md,abnormal\_iono,r})$.

To include the network information in the GBAS, the MDE of each network station must be translated into the MDG by the network at the location of the GBAS station(s) it protects. This step is achieved by means of Monte Carlo simulations, as explained in Section 5.

4 | DATA

As a representative monitoring network for the equatorial region, we selected eight stations situated in the state of São Paulo, Brazil. Figure 4 depicts the locations of these stations in blue. Public data are available for this network, whose stations belong to the Brazilian network for continuous GPS monitoring (RBMC), at a 15-s sampling rate for both L1 and L2 frequencies and GPS satellites (Instituto Brasileiro de Geografia e Estatística (IBGE), 2014). Nowadays, more stations are available in this area, and they provide data at a higher sampling rate. However, this work used the data available from 2014 because this year was a solar maximum and has been well studied in the literature. It should be noted that although a rate of 15 s is a low sampling rate, in this region, ionospheric perturbations (i.e., EPBs) also move at a lower speed than in other regions, e.g., Alaska, as shown by Caamano et al. (2021). Therefore, this work considered a 15-s sampling rate to be sufficient for this study. Owing to the limited availability of data recorded with L1/L5 frequencies and other constellations (e.g., Galileo) during active ionospheric conditions, real measurements on L1 and L2 frequencies from only the GPS constellation were used for this study.

Figure 4 shows the location of three airports in Brazil: São Paulo/Guarulhos – Governor André Franco Montoro International Airport (GRU) in red, Viracopos/Campinas International Airport (VCP) in yellow, and Guaratinguetá Airport (GUJ) in green. Considering EPB propagation characteristics (southwest to northeast), only the stations "neia," "spbo," and "poli" could potentially detect a gradient before either the GRU or VCP airport is affected. Although three is the minimum number of stations necessary to estimate the gradient parameters, there are not enough stations within a 200-km radius of either GRU or VCP — a limit we have set to ensure spatial coherence in the estimation of gradient parameters. Using stations beyond this distance could introduce errors due to possible changes in the

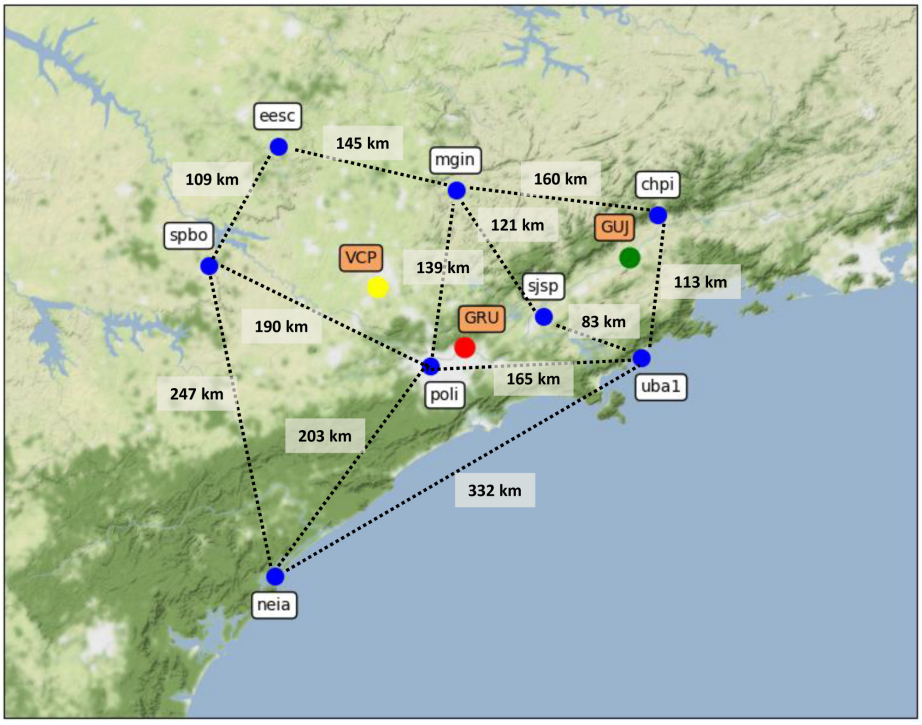

FIGURE 4 Locations of the network of monitoring stations and three airports in Brazil.

EPBs during propagation, as well as the risk of satellites rising or setting without capturing the gradient event.

Therefore, to adequately show the benefits of the network–GBAS methodology introduced in Section 3.1, the GUJ airport was selected as the location to simulate a GAST C station (CAT-I), as no real station is installed at this airport.

5 | SIMULATION SETUP

Once the MDE has been calculated for each station, the MDG of the network for a particular GBAS station location can be computed, ideally, by means of Monte Carlo simulations, in which the different parameters of the GBAS ionospheric threat model are varied until a representative number of samples is achieved. These simulations also allow one to consider those cases in which the locations of the ground stations are not similar to those of the IPPs owing to the low elevation of the satellites. The result of this simulation is an MDG expressed in mm/km that can serve as an input to the protected GBAS stations. In this section, we describe the simulation setup, and in Section 6.3, we describe the process for calculating the MDG based on these simulations and the network depicted in Figure 4.

In equatorial regions, anomalous ionospheric gradients are typically caused by EPBs; the model of these EPBs is more complex than the simple wedge model depicted in Figure 1. EPBs can be simplified and defined as two simple gradients (one downward, g_{iono_1}, with a width of w_{iono_1}, and one upward, g_{iono_2}, with a width of w_{iono_2}) separated by a zonal length, zl_{iono}, that move with a constant speed, v_{iono}, and direction, d_{iono}, over a "thin shell" layer at a height of 350 km above the Earth's surface (Yoon et al., 2017). Figure 5(a) shows the definition of the perturbation, including its propagation direction and the parameters used for its simulation. Note that the slopes and widths of both gradients could be different. The dimensions of the simulated EPB in the direction perpendicular to the direction of motion are considered to be infinite.

The previously defined simulation gradient parameters were varied within their ranges in the Brazilian threat model (see Table 1) up to a maximum slant additional delay of 35 m. The simulated trajectory was a straight line that formed a 58° angle with the North Pole, which is a good approximation of the modified dip latitude (MODIP) line of −30° in that area (see Figure 5(b)). The MODIP lines are lines with a constant MODIP angle, obtained by dividing the so-called geomagnetic DIP angle (i.e., the angle made with the horizontal by the Earth's magnetic field lines) by the cosine of the geographic latitude of the receiver. More details about the calculation of MODIP lines have been given by Blanch et al. (2018). EPBs are known to travel along the MODIP lines and therefore have a latitudinal variation (Blanch et al., 2018).

These synthetic perturbations were then added to the nominal slant ionospheric delays calculated with Equation (14) and the measurements recorded by the network of stations considered in this work (see Figure 4) during a nominal day (day 145 of year 2014, during which no anomalous ionospheric activity was observed). Note that the slope of the gradient was simulated in the vertical domain until the maximum value defined in the slant was reached for the Brazilian threat model and then multiplied by an obliquity factor to obtain the slant slopes. Therefore, in the case of low-elevation satellites, slant slopes that are much higher than the maximum slant slopes considered in the Brazilian threat model could be simulated. However, simulation cases that produced simulated slant slopes greater

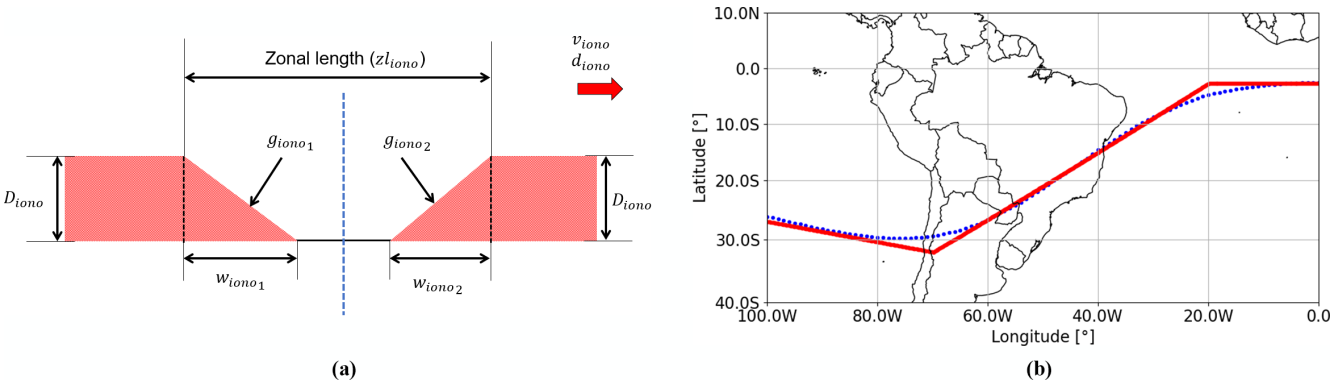

FIGURE 5 Simplified EPB model and trajectory used for simulations. (a) Simplified EPB model. (b) Trajectory of the simulated plasma bubble.
The blue dotted line depicts the MODIP line of −30°, and the red line depicts a linear curve fitting used in the simulation.

TABLE 1
Simulation Parameters for Brazil

Parameter	Minimum	Maximum	Step
$g_{iono,vert_1} = g_{iono,vert_2}$ [mm/km]	50	860	10
$w_{iono_1} = w_{iono_2}$ [km]	20	460	20
d_{iono} [°]	58	58	-
v_{iono} [m/s]	40	250	30
zl_{iono} [km]	90	750	220
$t_{iono,0}$ [GPS seconds of day]	0	82800	3600

than 860 mm/km were not considered. Moreover, although EPBs are known to occur during local nighttime (after sunset), they were simulated throughout the 24 h of day 145 to allow for more available satellite geometries. As a simplification, $g_{iono,vert_1} = g_{iono,vert_2}$ and $w_{iono1} = w_{iono2}$ were considered.

These exhaustive simulations should cover all reasonable variations of the gradient parameters, all reasonable IPP motions (especially with respect to gradient propagation), and all reasonable gradient onset times ($t_{iono,0}$). However, this type of simulation is computationally demanding because, for each variation of each gradient parameter, all reasonable variations of the other parameters must be simulated. In addition, an adequate step must be found for the variation of each gradient parameter that represents a significant variation of the parameter without losing important intermediate values. In this work, although the number of simulations performed was large (860,706 simulations) to demonstrate the methodology, these simulations were not exhaustive (e.g., the gradient onset time was simulated every hour; see Table 1), and they should be repeated if the method is to be implemented in real life.

6 | RESULTS AND DISCUSSION

As explained in Section 4, the GUJ airport was selected as the location for the GAST C station to protect. Therefore, the following sections show the results for a network protecting this particular airport.

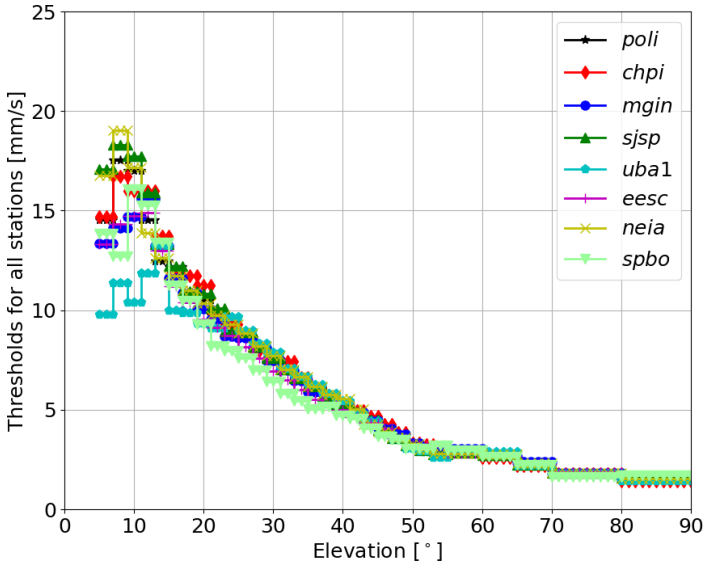

FIGURE 6 Detection thresholds for all stations considered in Brazil

6.1 | Detection Thresholds for Each Network Station

We used data from 24 h of 10 nominal days and the nominal 12 h (daytime) of 20 active days to derive the threshold for each network station. Additionally, we empirically selected a false-alert probability (P_{fa}) of 10^{-4} as an acceptable compromise for tests with real measurements from Brazil, considering the levels of noise and multipath and the number of statistically independent samples. Nevertheless, this value is likely not optimal owing to the limited data on which its selection was based, and optimization of its value will be investigated as part of future work.

Figure 6 shows the detection thresholds for all stations considered in Brazil (depicted in blue in Figure 4). Figure 6 shows that all network stations have similar performance for satellite elevations above 13°. Below that elevation, several satellites crossed the Appleton anomaly at different locations. The Appleton anomaly is a region of enhanced electron density located approximately 15°–20° north and south of the geomagnetic equator. Its formation is a result of the equatorial fountain effect, where ionized plasma is lifted at the magnetic equator and then redistributed along magnetic field lines to higher latitudes. This situation results in two crests of high electron density near the equator. The anomaly is most pronounced during the daytime and periods of high solar activity, but can be considered "nominal." The Appleton anomaly caused different nominal delays in satellites crossing it. These delays occurred for satellite elevations between 7° and 13°, where the thresholds are higher compared with those between 5° and 7°. In addition, the threshold for station "uba1" is slightly lower for satellite elevations below 13° because fewer measurements were available at these elevations for this station and therefore the maximum values of nominal ionospheric delays could not be reached. This fact resulted in a more sensitive performance of station "uba1," which could trigger more false alerts than the other stations for satellites at lower elevations.

6.2 | MDE for Each Network Station

The first step for obtaining the MDE per station is to compute the probability of missed detection per station $P_{md,abnormal\_iono,r}$, taking into account the

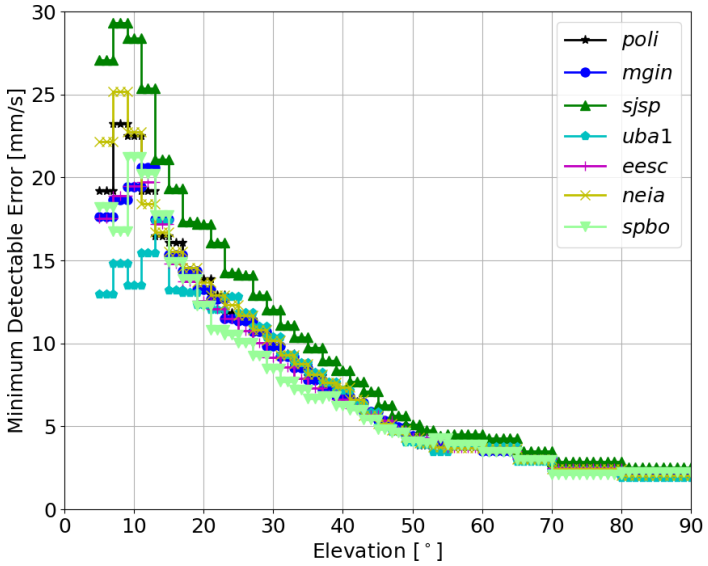

FIGURE 7 MDE for all stations considered in Brazil

propagation directions considered in the Brazilian threat model. As commented previously, EPBs, upon which the Brazilian threat model is based, do not propagate in all directions; rather, they typically move from west to east along lines of constant MODIP (Blanch et al., 2018). Therefore, stations "neia," "spbo," "poli," "eesc," "mgin," "sjsp," and "uba1" could detect an anomalous ionospheric gradient propagating along these MODIP lines in the area of interest before the gradient affects the GUJ airport (see Figure 4). Applying the methodology and values from Section 3.2, the network would assign $P_{md,abnormal\_iono,r} = 10^{-1}$ for six of the stations and $P_{md,abnormal\_iono,r} = 10^{-2}$ for one station to achieve the $P_{md,abnormal\_iono} = 1 \times 10^{-8}$ necessary to meet the integrity requirement. Of the available stations, station "sjsp" is the closest to the GUJ airport and therefore the most important for detecting ionospheric perturbations before they affect the simulated GBAS station. Additionally, the IPPs for this station will experience gradients most similar to those experienced by the simulated GBAS station given the proximity of this station. Therefore, station "sjsp" should have the lowest probability of missed detection among all monitoring stations considered. For this reason, we selected $P_{md,abnormal\_iono,sjsp} = 10^{-2}$ for "sjsp" and $P_{md,abnormal\_iono,r} = 10^{-1}$ for stations "neia," "spbo," "poli," "eesc," "mgin," and "uba1." Station "chpi" is located beyond the GUJ airport and thus would not be able to protect the airport from undetected EPBs owing to their propagation direction.

Figure 7 shows the MDE in mm/s (same units as the threshold) calculated for each station considered. As can be observed, the MDE is similar for all stations, with the exception of "sjsp," because a different $P_{md,abnormal\_iono,r}$ was selected for this station. The differences are smaller among the values for the other stations, especially for satellite elevations below 20°. This result arises because different stations have different noise and nominal ionosphere characteristics, as explained in Section 6.1.

6.3 | Computation of the MDG for GUJ Airport in Brazil

Once the MDE has been calculated for each station, the MDG of the network for a particular GBAS station location can be computed by following the simulation

steps explained in Section 5, which incorporate synthetic EPBs in the nominal real data.

With these data, we calculated $Itest_r^j$ for each station r and each satellite j following Equation (15). Next, the algorithm computed the MDG per satellite as follows. If the absolute value of $Itest_r^j$ corresponding to one of the stations, r, and one satellite, j, exceeds its corresponding MDE_r (see Figure 7) before the IPP belonging to the same satellite, j, and the simulated GBAS station is affected, that simulated ionospheric perturbation is guaranteed to be detected for that satellite with the required $P_{md,abnormal\_iono,r}$. However, the absolute value of $Itest_r^j$ may not exceed the MDE for any of the stations before the gradient affects the IPP of the same satellite and the simulated GBAS station. This situation could arise if the ionospheric perturbation generates a low $Itest_r^j$ because the gradient slopes are not high or because the relative speeds between the ionospheric gradient and the IPPs of the stations are low. In these cases, the network considers that this ionospheric perturbation could not be detected for that satellite with the required probability of missed detection, and the slant slope of this gradient is recorded.

We assumed different cases for calculating the MDG: (i) a conservative case, where we used the MDE for each station, as calculated in Figure 7, and assumed that if the signal was lost in one or more of the monitoring stations owing to scintillation, the GBAS was still able to track it, and (ii) an optimistic case, where we used the lowest MDE for all stations and assumed that, if the signal was lost in one or more of the closest monitoring stations owing to scintillation, the signal would also be lost at the GBAS ground station and therefore no missed detection would occur.

Once the simulation is complete, the recorded slant slope values measured by each satellite are sorted into elevation bins. The sizes of the elevation bins used are 2° between 5° and 55° of elevation, 5° between 55° and 70° of elevation, and 10° between 70° and 90° of elevation. These different binning sizes are used to account for the different magnitudes of noise and multipath with elevation. The algorithm then selects the maximum slope value in mm/km for each bin, regardless of which satellite experienced it, as the MDG for each elevation bin.

Figure 8 shows the maximum undetected (i.e., with the required probability of missed detection) gradient slant slopes in mm/km per elevation bin (black stars)

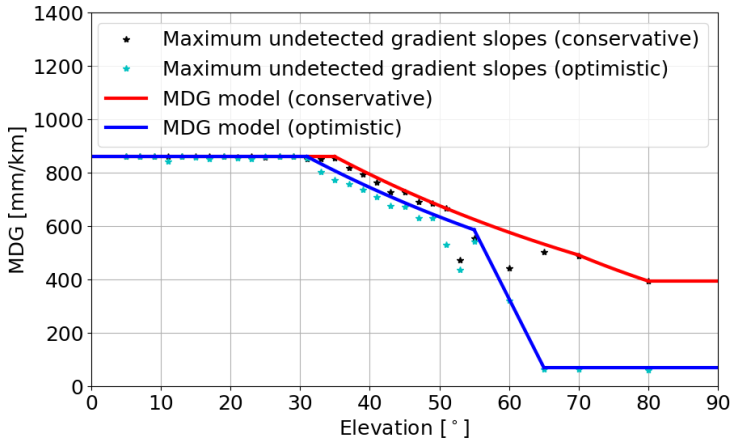

FIGURE 8 MDG calculated for a simulated GBAS station situated at the GUJ airport. The black stars show the maximum undetected gradient slant slopes per elevation bin among all simulations in the conservative case, and the cyan stars show the maximum undetected gradient slant slopes in the optimistic case. The red lines show a curve fitting to the black stars, and the blue lines show a curve fitting to the cyan stars.

when considering the conservative assumptions mentioned earlier and the maximum undetected gradient slant slopes (cyan stars) when considering the optimistic assumptions. These points indicate that at least one gradient with that slope was not detected with the required probability of missed detection by any station for a particular satellite before the gradient affected the IPP for the same satellite and the GUJ airport.

As can be seen, for the conservative case, up to an elevation of 35°, ionospheric gradients of the same size as the conservative threat model (860 mm/km) affected at least one satellite visible at the GUJ airport without being previously detected with the required probability of missed detection by any of the stations. Most of these points belonged to undetected gradient slopes produced during the simulation with the minimum front speed considered in the Brazilian threat model, 40 m/s. This result occurred for several reasons. In some cases, the relative speeds between the IPPs and the simulated ionospheric perturbations were low; thus, the absolute values of $Itest_r^j$ were not sufficient to exceed the corresponding MDE_r values. This was especially the case when the IPPs moved in the same direction as the simulated ionospheric perturbations. Furthermore, there were cases in which a satellite rose above the elevation mask at almost the same time that the simulated ionospheric disturbance affected the GUJ airport. In these cases, the ionospheric disturbance affected the IPP corresponding to the GUJ airport and that specific satellite, whereas the other stations did not detect it because the corresponding satellite was not visible when the disturbance passed over them. This problem was aggravated by the presence of gaps in the data from the different stations, especially from the "uba1" station. These data gaps caused some ionospheric disturbances to go undetected because the measurements from the stations that would have protected the GUJ airport from these disturbances were not available at these times. Moreover, the maximum undetected slope values for satellite elevations between 51° and 70° are lower than what would be expected given the values for the other elevation bins. The reason for this result is that in the cases examined during the simulations, higher relative speeds between the simulated ionospheric perturbations and the IPPs corresponding to the satellites at these elevations were found; thus, perturbations with lower slopes were more easily detected, compared with results for lower elevations. If exhaustive simulations considering smaller steps for the variation of gradient parameters (e.g., gradient onset time) were performed, it is possible that larger values would be found for these maximum undetected gradient slopes, especially for these satellite elevations.

In the optimistic case, lower MDG values could be achieved owing to the lower MDE values used in each station and the assumption that losing the signal in one or more of the closest monitoring stations would also lead to a loss of signal at the same time for the GBAS station. Therefore, fewer missed detections occurred in the optimistic case.

Note that, for this analysis, detections from non-GPS satellites whose IPPs are close to the IPPs under study have not been considered. Including this information could be beneficial, especially if other satellite constellations are available. These additional satellites could be considered for the detection of anomalous ionospheric gradients and could be used for protecting nearby GPS satellites, making the overall MDG less conservative.

Finally, to introduce the obtained MDG in the PDGS algorithm, a model based on the black stars and a model based on the cyan stars from Figure 8 were derived. These models are represented by red and blue lines in Figure 8 and can be described by the equations in Tables 2 and 3, respectively.

TABLE 2
Conservative Model for the MDG

MDG in slant (conservative) [mm/km]	Elevation [°]
$g_{iono} = 860$	$\theta^j \leq 35°$
$g_{iono} = 860 \cdot e^{-0.016 \cdot (\theta^j - 35°)}$	$35° < \theta^j \leq 51°$
$g_{iono} = 665.9 \cdot e^{-0.016 \cdot (\theta^j - 51°)}$	$51° < \theta^j \leq 70°$
$g_{iono} = 491 \cdot e^{-0.022 \cdot (\theta^j - 70°)}$	$70° < \theta^j \leq 80°$
$g_{iono} = 393$	$\theta^j > 80°$

TABLE 3
Optimistic Model for the MDG

MDG in slant (optimistic) [mm/km]	Elevation [°]
$g_{iono} = 860$	$\theta^j \leq 31°$
$g_{iono} = 860 \cdot e^{-0.016 \cdot (\theta^j - 31°)}$	$31° < \theta^j \leq 55°$
$g_{iono} = 585.77 - 51.58 \cdot (\theta^j - 55°)$	$55° < \theta^j \leq 65°$
$g_{iono} = 70$	$65° < \theta^j \leq 90°$

6.4 | GBAS Availability Assessment Under Nominal Conditions at GUJ Airport

To evaluate the performance of our network–GBAS methodology on a nominal ("calm") day, we used data from day 145 of year 2014 (i.e., May 25, 2014), which was a day without significant ionospheric activity.

Once valid MDGs (conservative and optimistic) were derived for the network coverage area, the network–GBAS algorithm calculated the gradient slope parameter (g_{iono}) to be used at each epoch within the PDGS considering the network's output in real time. For this purpose, the network–GBAS algorithm calculated the test statistics $(Itest_r^j)$ from Equation (15) using the real measurements recorded during the 24 h of this day for all GPS satellites. Then, the algorithm compared the absolute value of each $Itest_r^j$ with the respective detection thresholds depicted in Figure 6. During this day, the network did not detect any anomalous ionospheric perturbations for any of the satellites or stations. As a result, the network–GBAS indicated the use of the MDG at all times of the day. Note that in this case, the objective is to detect the gradients satisfying the probability of false alert and not to calculate the MDG. Therefore, the detection thresholds have been used here instead of the MDE.

6.4.1 | Results of EPB Threat Mitigation via PDGS Using the Network–GBAS Methodology on a Calm Day

The next step was to calculate the inflation factors for the selected day using the PDGS algorithm adapted for Brazil, as proposed by Yoon et al. (2019). PDGS requires different parameters as input: the ground, air, tropospheric, and ionospheric residual error models, the satellite geometries to be simulated, the DH distance (x_{Air}), and the values of the threat model.

For the ground error model, the GBAS approach designator C curve (McGraw et al., 2000) was selected, as this corresponds to the level of noise and

multipath expected in a real GBAS ground station. For the airborne error model, σ_{pr_air}, the strategy presented by Yoon et al. (2019) was followed. On one hand, the more severe airborne error model was selected for the MIEV calculation (i.e., airborne noise model, σ_n, with airborne accuracy designator A as described in Section 3.6.8.2 of the standards reported by the International Civil Aviation Organization (2017)). On the other hand, the theoretical minimum airborne error model (i.e., $\sigma_n = 0$) was selected for computing the VPLs. The tropospheric residual error was computed as described in Section 2.3.12.2 of the standards reported by RTCA (2017). Additionally, a broadcast σ_{vig} of 14 mm/km (without inflation) was used for daytime conditions, as proposed by Chang et al. (2021), and a hypothesized σ_{vig} of 15 mm/km (without inflation) was applied for nighttime conditions, as proposed by Yoon et al. (2019). The total ionospheric error (σ_{iono}) was calculated as in Section 2.3.12.3 of the standards reported by RTCA (2017), and the total uncertainty of the residual differential pseudorange error (σ_{GBAS}) was computed using Equation (2).

The PDGS algorithm adapted for Brazil requires a knowledge of the possible range of EPB propagation directions, in order to discard pairs of satellites that are physically improbable to be affected at the same time, as explained by Yoon et al. (2019). For this purpose, an EPB direction of 58° measured in the clockwise direction from the North Pole was selected, as discussed in Section 5. Only this direction was considered because it corresponds to the line of $MODIP = -30°$, which is close to the network under study. However, a more exhaustive study should consider a range of directions around this mean value (e.g., between 43° and 73° for the mean direction of 58°) selected from sufficient estimates of the typical directions of EPBs in this region.

Furthermore, the almanac that describes the Standard 24 satellite GPS constellation (Section 3.2 and Table A.2-1. in the standards of the U.S. Department of Defense (2008)) was used to compute satellite geometries at selected times on the selected day. A constant speed of 70 m/s was selected for the approaching aircraft, and the DH distance, x_{Air}, was assumed to range from 1 to 4 km (in 1-km increments) from the GBAS ground facility to obtain results comparable to those obtained by Yoon et al. (2019) for Rio de Janeiro, which is geographically close to the GUJ airport. Unlike the study by Yoon et al. (2019), only cases for which the aircraft was exactly situated at the different DHs were simulated. The reason for this is that these cases typically require the greatest inflation of the integrity parameters, as both the VAL and TEL, which increase with the distance to the DH, have the lowest values.

Four different simulations were conducted with the PDGS algorithm, generating the required inflation factors every 15 s for over 24 h. In each simulation, the g_{iono} parameter used for calculating the EPB ionosphere-induced range errors in PDGS corresponded to the following: (i) the elevation-dependent maximum slope from the Contiguous United States (CONUS) threat model for daytime (06:00 to 18:00 local time at GUJ), (ii) the 860-mm/km maximum slope from the Brazilian threat model for nighttime (18:00 to 06:00 local time at GUJ), (iii) the slope indicated by the network–GBAS algorithm as output in real time for nighttime (18:00 to 06:00 local time at GUJ) in the conservative case, and (iv) the slope indicated by the network–GBAS algorithm as output in real time for nighttime (18:00 to 06:00 local time at GUJ) in the optimistic case.

Within PDGS, two VPLs were considered: the VPL under the fault-free hypothesis, VPL_{H0}, and the vertical ephemeris PL, *VPB*. PDGS uses the maximum of these two values to compute inflation factors. For the calculation of VPL_{H0} with Equation (1), a fault-free missed detection multiplier, k_{ffmd}, of 5.847 was used, assuming that four ground subsystem reference receivers are installed. For the

calculation of VPB with Equation (7), an ephemeris missed detection multiplier, k_{md_e}, of 3.80 and an ephemeris decorrelation parameter for satellite j, P^j, of 0.00018 were used (Yoon et al., 2019).

Figure 9(a) shows the maximum inflation factors for both σ_{vig}, I_{vig}, and σ_{pr_gnd}, I_{gnd}, for the four simulations at each epoch. During the daytime, σ_{pr_gnd} did not need to be inflated because the inflated σ_{vig} did not reach the maximum allowable limit of 25.5 mm/km (the maximum allowable I_{vig} is 1.82 considering $\sigma_{vig} = 14$ mm/km). This result occurred because the CONUS ionospheric threat model, which is used during the day, is significantly less conservative than the Brazilian ionospheric threat model; therefore, fewer satellite geometries had to be discarded within the PDGS algorithm.

During the nighttime, inflating only σ_{vig} was not sufficient to completely remove all potentially unsafe satellite geometries when using both the conservative Brazilian threat model (860 mm/km, blue line) and the MDG (magenta line for the conservative case and cyan line for the optimistic case). In the three cases, I_{vig} reached its maximum allowable value of 1.7 (corresponding to $\sigma_{vig} = 15$ mm/km); thus, additional inflation of σ_{pr_gnd} was required. However, the inflation factors required when using the MDG, especially in the optimistic case, were considerably lower than those obtained when using the Brazilian threat model, especially I_{gnd}. Furthermore, far fewer epochs required inflation of the σ_{vig} and σ_{pr_gnd} parameters. These epochs, in which both the I_{vig} and I_{gnd} values calculated with the MDG were also high, corresponded to particularly weak satellite geometries. In these satellite geometries, there were cases in which satellites with high S-projection factors, s_{apr_vert}, (see Equation (3) in Section 2.1) were at elevations below 35°. For satellite elevations below 35° for the conservative case and below 31° for the optimistic case, the MDG values are the same as those of the Brazilian threat model; thus, the IEVs for certain subsets of satellites within PDGS were high. This situation led to considerable inflation of the integrity parameters to protect against particularly weak satellite geometries. Nevertheless, even in these

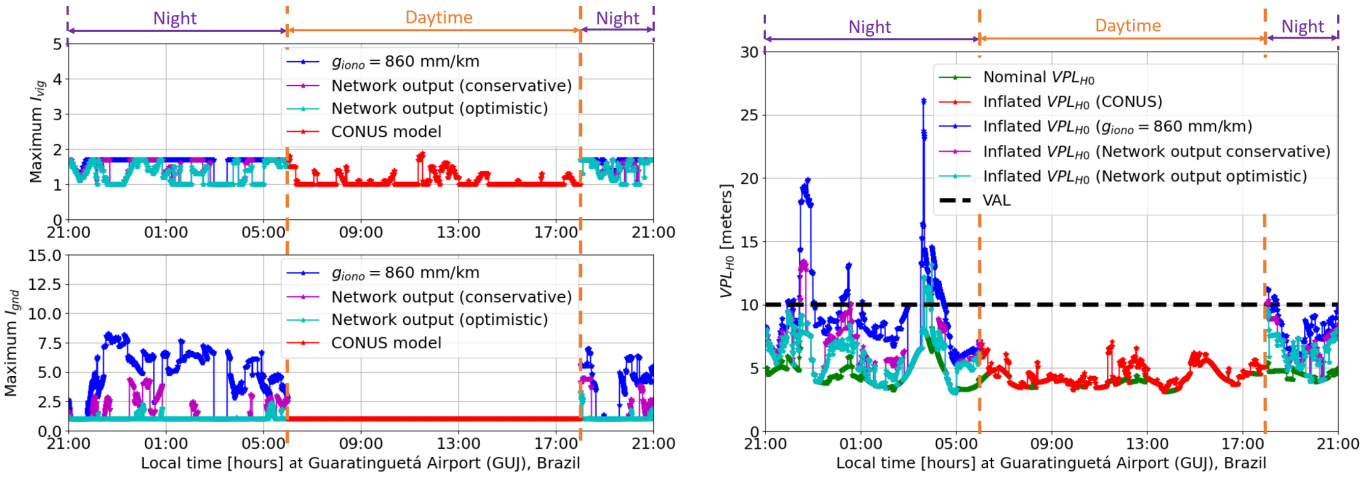

FIGURE 9 Inflation factors and VPLs calculated at each epoch (day 145 of year 2014). (a) Maximum inflation factors for σ_{vig}, I_{vig}, and for σ_{pr_gnd}, I_{gnd}, (b) VPL_{H0} calculated by applying I_{vig} and I_{gnd} from Figure 9(a).
The CONUS threat model (red line) was used during daytime (06:00–18:00 local time), and the Brazilian threat model (blue line) and the MDGs (magenta line for the conservative case and cyan line for the optimistic case) were used during nighttime (18:00–06:00 local time). The VAL in Figure 9(b) is represented by a black dashed line.

cases, the overall combination for the different satellite subsets within the PDGS resulted in lower inflation when using the MDGs than when using the conservative Brazilian threat model.

During normal GBAS operation, the ground station broadcasts the inflated σ_{vig} and σ_{pr_gnd} integrity parameters to approaching aircraft. These aircraft calculate the VPLs with the transmitted integrity parameters, thus eliminating all potentially hazardous satellite geometries. Figure 9(b) shows the nominal VPL_{H0} and the inflated VPL_{H0} computed at a 4-km DH distance for the all-in-view satellite geometries during the 24 h of the selected day. Note that a 4-km DH distance was selected for this evaluation because it was the largest DH distance considered in the PDGS algorithm and thus the most conservative, as the VPL increases with distance to the GBAS ground station. Furthermore, only VPL_{H0} was considered because it is typically larger than VPB at these DH distances. This last statement was verified by a simulation with PDGS, where, for the DH distances considered, the highest VPL values were always achieved by VPL_{H0}.

Figure 9(b) depicts the VAL value at the DH distance (black dashed line), which is equal to 10 m. A green line shows the nominal VPL_{H0}, which was based on the uninflated σ_{vig} and σ_{pr_gnd} parameters. As can be seen, even without inflation, the nominal VPL_{H0} grew above 7 m, reaching a value higher than usual, between 22:28 and 22:55 local time and between 03:33 and 03:59 local time. As explained above, this result was due to the fact that, at these local times, the satellite geometries were especially weak. The red line shows the inflated VPL_{H0} during the daytime based on the σ_{vig} and σ_{pr_gnd} parameters inflated with the CONUS threat model. In this case, the inflated VPL_{H0} (red line) was higher than the nominal VPL_{H0} in some epochs, especially for the cases in which the satellite geometries were weak. However, all points of the red line were below the VAL; therefore, the GBAS availability would have been 100% during the daytime for approaching aircraft tracking all satellites in view. Note that the system availability was assessed based on the fraction of the time that the VPL was below the VAL.

The blue line in Figure 9(b) shows the "worst-case" inflated VPL_{H0} during the nighttime, which used the σ_{vig} and σ_{pr_gnd} parameters inflated with the current Brazilian threat model (with a maximum slope of 860 mm/km). The VPL was higher than the VAL for long periods of time during the night, causing the overall GBAS availability to drop to 79.5%. Finally, the magenta and cyan lines show the inflated VPL_{H0} that used the MDGs depicted in Figure 8 during the nighttime. Using the MDG values instead of the more conservative threat model allowed a reduction in VPL at practically all epochs. At some epochs, the inflated VPL_{H0} values with both MDGs were still higher than the VAL due, again, to the combination of weak geometries with the high MDG values for low elevations. Nevertheless, the GBAS availability increased to 94.6% when using the MDG in the conservative case and to 97.95% when using the MDG in the optimistic case.

6.5 | GBAS Availability Assessment Under Active Conditions at GUJ Airport

To evaluate the performance of the network–GBAS methodology on active ionospheric days, we selected part of day 68 and day 69 of year 2014 (i.e., March 9 and 10, 2014). Part of day 68 was included to capture the onset of an ionospheric storm, which continued into day 69.

This study followed the same process as in Section 6.4. First, the network–GBAS algorithm calculated the test statistics $(Itest_r^j)$ from the real measurements; then,

it compared the test statistics with their corresponding detection thresholds. However, in contrast to the results of Section 6.4, multiple satellites were simultaneously affected by large EPBs and/or scintillation during the nighttime hours of these days. Figure 10 shows the network output for each of the visible satellites for the days under study.

The network output was either "0" or "1" depending on the real-time ionospheric conditions. When the network did not detect any ionospheric disturbance at a time instant t for a specific satellite, the network output was "0" for that time and that satellite. In these cases, the network indicated the use of the MDG for that satellite as the input to PDGS. When the network detected an ionospheric disturbance at a time instant t for a specific satellite, the network output was "1" for that time and that satellite. In these cases, the network searched its database for the estimated and overbounded gradient slope for that particular satellite. If this value was available from multiple stations, the network indicated the use of the maximum estimated and overbounded gradient slant slope among all stations for that satellite as the input to PDGS. This was the case for satellite G31, for which the network managed to estimate and overbound the slope of the actual detected ionospheric gradient in real time. The maximum estimated and overbounded value of the gradient slope was 727.71 mm/km. The process for estimating and overbounding the slope of the gradients measured by this network has been explained by Caamano et al. (2025) and, therefore, is not repeated in this work. If the value of the estimated and overbounded slope was not available for the satellite of interest, either the algorithm had not converged yet or it had not been able to estimate this parameter for other reasons (e.g., scintillation, false alerts, data gaps, etc.). In these cases, the network indicated the use of the current conservative Brazilian threat model as the input to PDGS.

As explained above, the work by Yoon et al. (2019) did not distinguish between nominal and active ionospheric conditions beyond using two different threat models, CONUS and Brazil, for daytime and nighttime, respectively. However, the network–GBAS algorithm can distinguish between affected and unaffected satellites and indicates which gradient slope should be used at which time periods. As shown in Figure 10, this feature is advantageous with respect to the current solution given that, from approximately 2:48 to 19:30 local time (for both days), none of the satellites detected ionospheric perturbations. Therefore, in the worst-case operational scenario — where estimated gradient slopes may not be available — the network–GBAS algorithm would provide at least 4.5 h per day of improvement during nighttime compared with the solution proposed by Yoon et al. (2019).

6.5.1 | Results of EPB Threat Mitigation via PDGS Using the Network–GBAS Algorithm on an Active Day

This section evaluates the performance of the PDGS algorithm when using the network–GBAS approach during an active ionospheric day (day 69 of year 2014) and part of the previous day. This study conducted the same four simulations as in Section 6.4 with the PDGS algorithm generating the required inflation factors every 15 s for more than 24 h. In this case, the slope indicated by the network–GBAS algorithm as output in real time for nighttime (18:00 to 06:00 local time at GUJ) was different from the MDGs when the network detected a gradient.

The remaining parameters selected for PDGS in this section were identical to the parameters selected for Section 6.4 except for the days of the year for which the satellite geometries were calculated, corresponding to part of day 68 and the full

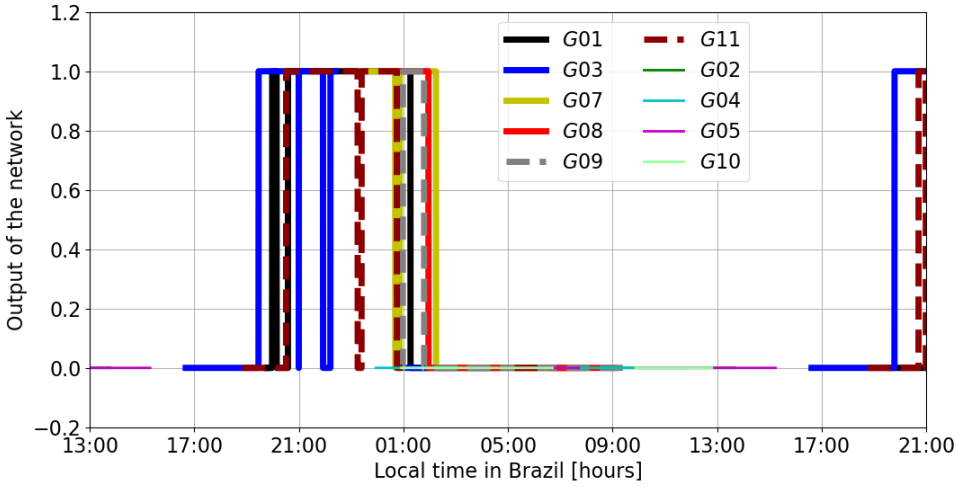

(a)

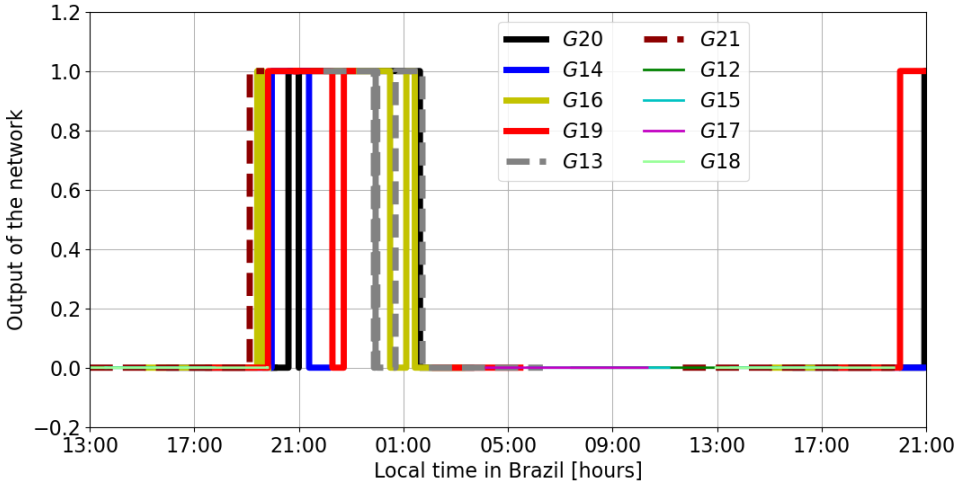

(b)

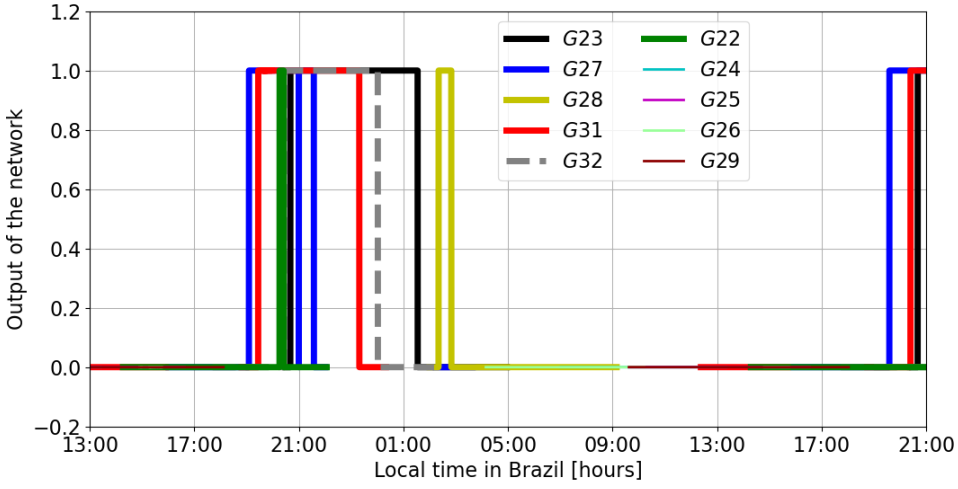

(c)

FIGURE 10 Output of the network–GBAS algorithm for all-in-view satellites (represented in different colors and types of lines) during part of day 68 and all of day 69 of year 2014. (a) Satellites G01 to G11. (b) Satellites G12 to G21. (c) Satellites G22 to G32.
When the output is "0," the network of stations did not detect any ionospheric perturbations for that specific satellite; when the output is "1," the network detected an ionospheric perturbation with at least one of its stations for that satellite.

day 69 of year 2014. In this section, the process for calculating the inflation factors and the VPLs is also analogous to the process followed in Section 6.4; therefore, an explanation is not repeated in this section.

Figure 11 shows the maximum inflation factors for both σ_{vig}, I_{vig}, and σ_{pr_gnd}, I_{gnd}, for the four simulations at each epoch. During the daytime, σ_{pr_gnd} did not need to be inflated because the inflated σ_{vig} did not reach the maximum allowable limit of 25.5 mm/km. During the nighttime, inflating only σ_{vig} was not sufficient to completely remove all potentially unsafe satellite geometries when using both the conservative Brazilian threat model (860 mm/km, blue line) and the network output (magenta and cyan lines). In both cases, I_{vig} reached its maximum allowable value of 1.7 (corresponding to $\sigma_{vig} = 15$ mm/km); thus, additional inflation of σ_{pr_gnd} was required. As in the nominal day, the inflation factors required when using the network output were considerably lower than when using the Brazilian threat model most of the time, especially for I_{gnd}. This behavior was observed during nighttime hours when the network did not detect any ionospheric gradients for any satellites or for only a few satellites simultaneously. An exception occurred at approximately 22:15–23:51 local time, when the inflation factors derived from the network outputs and those obtained using the conservative Brazilian threat model were nearly identical. The reason for this result was that between these local times, almost all satellites in view were simultaneously affected by different EPBs, as shown in Figure 10. Therefore, the network indicated the use of the conservative Brazilian threat model for all of the satellites, obtaining the same result as the blue line.

The next step in computing the VPLs involves determining the set of smoothed satellites and the corresponding satellite geometries at the user side. In the nominal

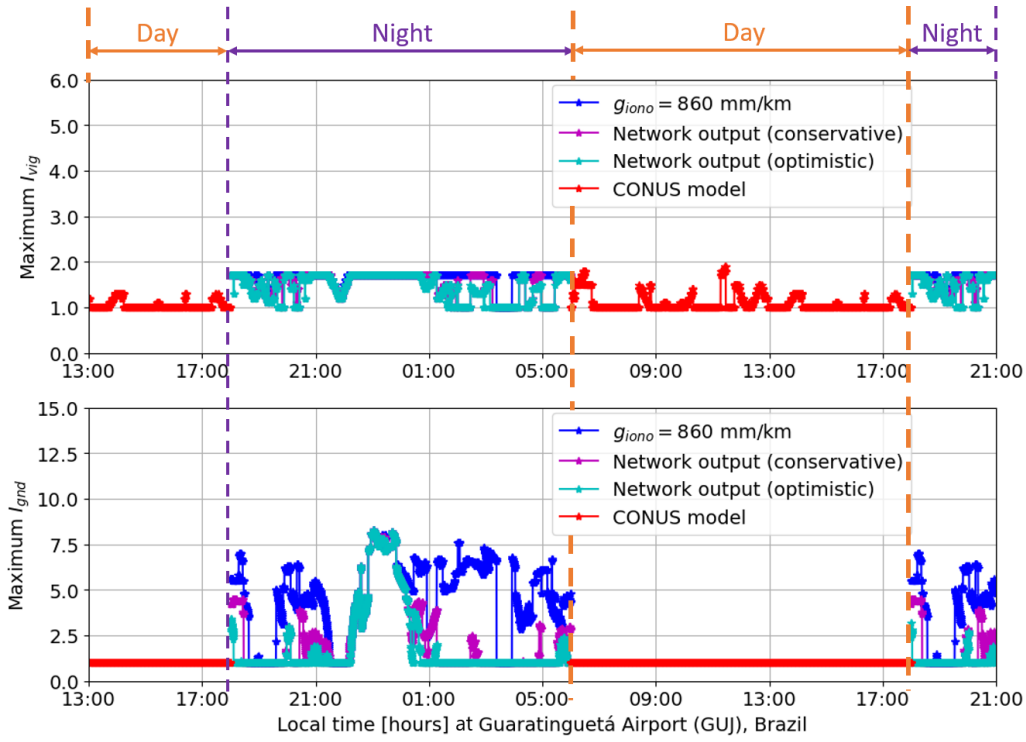

FIGURE 11 Maximum inflation factors for σ_{vig}, I_{vig}, and for σ_{pr_gnd}, I_{gnd} (day 68 and 69 of year 2014).
The CONUS threat model (red line) was used during daytime (06:00–18:00 local time), and the Brazilian threat model (blue line) and the MDGs (magenta line for the conservative case and cyan line for the optimistic case) were used during nighttime (18:00–06:00 local time).

case discussed in Section 6.4, scintillation was absent, and the station network, simulated ground station, and simulated user shared nearly identical satellite geometries — with minor differences arising from the convergence time of the smoothing filters in the GBAS station and the user, but not in the network, which does not use smoothed measurements. In contrast, during the active nighttime period with ionospheric activity, the situation changed. Under these conditions, the number of tracked satellites differed from the number of smoothed satellites, particularly when continuous phase losses occurred as a result of scintillation. This behavior is illustrated in Figure 12, which shows the number of satellites visible/tracked by the user (blue), the number of simultaneously affected satellites detected by the network (red), and the number of satellites smoothed by the user (green), assuming steady-state conditions of the smoothing filters at twice the smoothing time constant (i.e., 200 s). As shown, even when multiple satellites were simultaneously affected by ionospheric anomalies, a substantial number of satellites remain tracked, smoothed, and available for user operations.

It is important to note, however, that the results related to satellite tracking under scintillation conditions may be somewhat pessimistic in this study. Because actual pseudorange and carrier-phase measurements were not available for the simulated GBAS station at GUJ (or the user), the information on the number of tracked and smoothed satellites was derived from one of the network stations (i.e., "poli"), which is located near the GUJ site. Consequently, this analysis assumes that the tracking performance of the GBAS ground station and the user is equivalent to that of a public reference station in Brazil. This assumption is likely conservative, as the receivers used in GBAS ground and airborne systems are expected to exhibit different tracking behaviors. This simplification will be refined in future work through the use of more realistic receiver tracking models.

Figure 13 shows the nominal VPL_{H0} and the inflated VPL_{H0} computed at a 4-km DH distance for the smoothed satellites during the 24 h of day 69 of year 2014 and a portion of the previous day. The green line shows the nominal VPL_{H0}, which used the uninflated σ_{vig} and σ_{pr_gnd} parameters. As can be seen, the nominal VPL_{H0} had a similar range of values during the time period under study, which indicates that, during these days, the satellite geometries were "stronger" than during day 145 of 2014. The red line shows the daytime results for the inflated VPL_{H0} that used the σ_{vig} and σ_{pr_gnd} parameters inflated with the CONUS threat model. In this case, the inflated VPL_{H0} (red line) was higher than the nominal VPL_{H0} (green

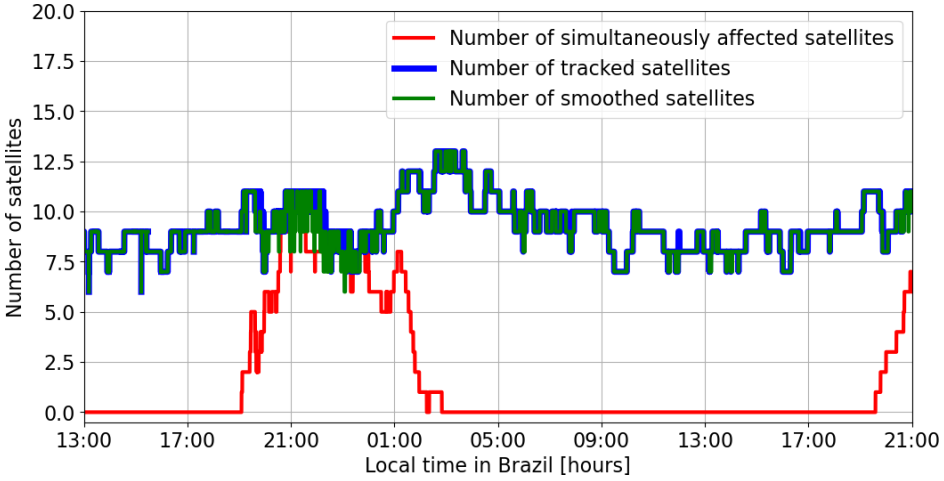

FIGURE 12 Number of tracked satellites (blue), simultaneously affected satellites (red), and smoothed satellites (green).

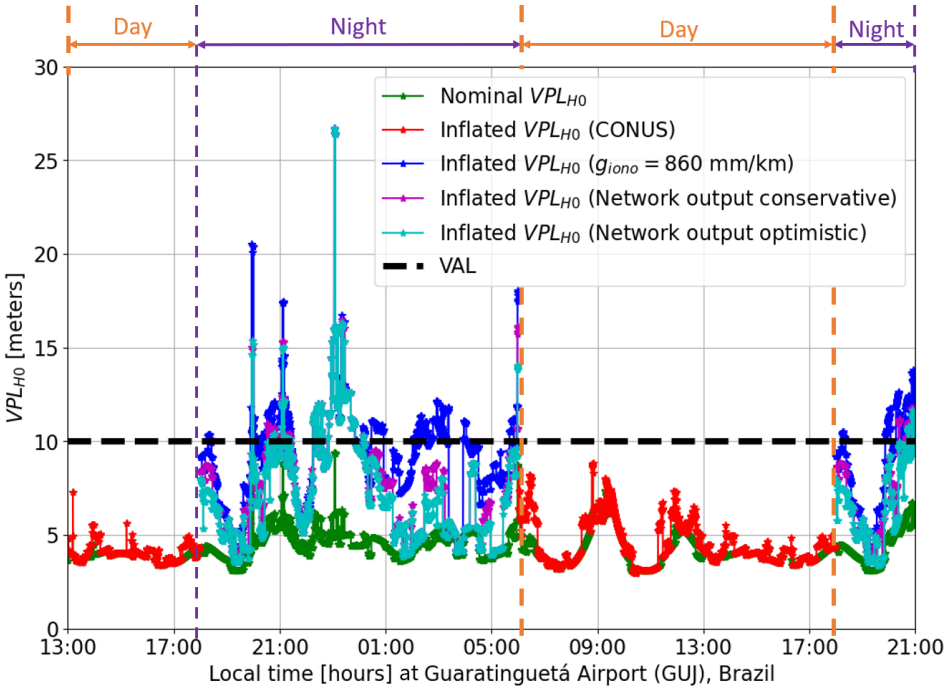

FIGURE 13 VPLs calculated at each epoch (part of day 68 and day 69 of year 2014). The CONUS threat model (red line) was used during daytime (06:00–18:00 local time), and the Brazilian threat model (blue line) and the MDGs (magenta line for the conservative case and cyan line for the optimistic case) were used during nighttime (18:00–06:00 local time). The VAL is represented by a black dashed line.

line) at some epochs, especially for cases in which the satellite geometries were weaker than for the remaining epochs. However, all points of the red line were below the VAL; therefore, the GBAS availability was also 100% during the daytime for the active days.

The blue line of Figure 13 shows the "worst-case" inflated VPL_{H0} during the nighttime, which used the σ_{vig} and σ_{pr_gnd} parameters inflated with the current Brazilian threat model (860 mm/km). In this case, the VPL exceeded the VAL for long periods of time during the night, causing the overall nighttime CAT-I GBAS availability to drop to 59.77% (based on two days of nighttime measurements). Finally, the magenta and cyan lines show the inflated VPL_{H0} values based on the network outputs depicted in Figure 10 during the nighttime. Using the slope values indicated by the network in both the conservative and the optimistic case instead of the more conservative threat model allowed a reduction in VPL at practically all epochs when the network output was lower than the worst-case gradient. At some epochs, the VPL_{H0} inflated with the slope indicated by the network was higher than the VAL, owing to the network's indication to use the more conservative threat model. This result occurred when the network detected different ionospheric gradients affecting multiple satellites simultaneously. Nevertheless, the network–GBAS algorithm increased the CAT-I GBAS nighttime availability to 79.83% when using the MDG for the conservative case and to 84.13% when using the MDG for the optimistic case. In this case, the difference between the MDG in the conservative and optimistic cases was small. This result was due to the fact that the performance here was driven by the times during the nighttime for which both cases had to use the Brazilian threat model because almost all satellites were simultaneously affected. Additionally, the still-conservative values of both MDGs for low-elevation satellites also contributed to this effect (see Figure 8).

7 | CONCLUSION

As discussed throughout this work, our approach differs significantly from others in the literature in that we propose using a regional ground-based network of GNSS stations instead of relying on satellite-based augmentation system (SBAS) information or ionospheric indices. This choice is motivated by several practical and technical considerations. First, an SBAS solution is currently not feasible in Brazil owing to the lack of its own operational SBAS constellation or regional augmentation network for providing precise GNSS corrections locally. Second, even if an SBAS were available, its spatial resolution could potentially be insufficient to capture the highly localized ionospheric irregularities common in equatorial regions, such as EPBs. Moreover, SBAS availability itself may degrade during strong scintillation events, precisely when the integrity of GNSS-based systems is most critical. In contrast, ground networks are flexible and can leverage existing infrastructure or can be expanded relatively easily to enhance coverage in key areas.

The case of using ionospheric indices (as discussed in the Section 1) also presents challenges — not only in terms of integrating the indices into the PDGS or GBAS, but also regarding data security. The network–GBAS approach addresses this challenge by allowing the GBAS service provider or the relevant government authority to also manage the monitoring network, ensuring secure (e.g., encrypted) transmission of protected information and reliability of the data sources.

In this work, we not only demonstrated the feasibility of the network–GBAS concept but also evaluated its performance using existing networks, which were not originally designed or optimized for this purpose. Despite these limitations, our results show a significant improvement in CAT-I GBAS availability during nighttime conditions. Under nominal conditions, nighttime availability increased from 79.5% (current solution) to 94.6% (conservative MDG) and 97.95% (optimistic MDG). Under active ionospheric conditions, nighttime availability improved from 59.77% to 79.83% and 84.13%, respectively.

Although these results show clear benefits, neither solution achieved the 99% availability required for CAT-I precision approaches. This is primarily due to a loss of lock of signals during scintillation as well as suboptimal satellite geometries and conservative MDG values, arising from the fact that the current network was not tailored for this application. Therefore, future improvements should focus on the intentional design and deployment of monitoring networks specifically adapted to protect individual airports or regions.

To support such efforts, we offer the following recommendations for the design of future network–GBAS monitoring networks:

- GNSS receivers robust to scintillation and capable of adequate sampling rates should be used. For instance, in high-latitude regions such as Alaska, a rate of at least 10 Hz is advisable, whereas in Brazil, a lower rate (e.g., 5 Hz) may suffice, provided that the rate aligns with the real-time requirements of the GBAS station.
- The network topology should be adapted to the regional ionospheric conditions. Specifically, the baselines between stations should correspond to the local correlation radius of ionospheric perturbations, i.e., the distance over which perturbations remain similar in shape, magnitude, and size. Moreover, the positioning of stations should consider the typical propagation direction of ionospheric fronts. As explained in Section 4, the network configuration was not optimal for covering the GRU or VCP airports. Only the minimum number

of stations was available before the ionospheric fronts could reach these airports, and the distances between stations exceeded the defined correlation radius. While the correlation radius value selected for this work is somewhat optimistic in Brazil — it typically ranges between 50 and 100 km — we were constrained to use the available infrastructure, which limited the availability of usable stations.

REFERENCES

Blanch, E., Altadill, D., Juan, J. M., Camps, A., Barbosa, J., González-Casado, G., Riba, J., Sanz, J., Vazquez, G., & Orús-Pérez, R. (2018). Improved characterization and modeling of equatorial plasma depletions. *Journal of Space Weather and Space Climate*, *8*, A38. https://doi.org/10.1051/swsc/2018026

Caamano, M., Juan, J., Felux, M., Gerbeth, D., Gonzalez-Casado, G., & Sanz, J. (2021). Network-based ionospheric gradient monitoring to support GBAS. *NAVIGATION*, *68*(1), 135–156. https://doi.org/10.1002/navi.411

Caamano, M., Juan, J., Sanz, J., & Pullen, S. (2025). Overbounding of near real-time estimated ionospheric gradient slope in low latitude regions. *NAVIGATION*, *72*(1). https://doi.org/10.33012/navi.689

Chang, H., Yoon, M., Pullen, S., Marini-Pereira, L., & Lee, J. (2021). Ionospheric spatial decorrelation assessment for GBAS daytime operations in Brazil. *NAVIGATION*, *68*(2), 391–404. https://doi.org/10.1002/navi.418

Datta-Barua, S., Lee, J., Pullen, S., Luo, M., Ene, A., Qiu, D., Zhang, G., & Enge, P. (2010). Ionospheric threat parameterization for local area Global-Positioning-System-based aircraft landing systems. *Journal of Aircraft*, *47*(4), 1141–1151. https://doi.org/10.2514/1.46719

Eurocae. (2013, March). *ED-114A, Minimum operational performance specification for global navigation satellite ground based augmentation system ground equipment to support category I operations* (E. O. for Civil Aviation Equipment, Ed.).

Hernández-Pajares, M., Juan, J., & Sanz, J. (2006). Medium-scale traveling ionospheric disturbances affecting GPS measurements: Spatial and temporal analysis. *Journal of Geophysical Research: Space Physics*, *111*(A7). https://doi.org/10.1029/2005JA011474

Instituto Brasileiro de Geografia e Estatística (IBGE). (2014). *Brazilian network for continuous monitoring of GPS (RBMC)*. https://www.ibge.gov.br/

International Civil Aviation Organization. (2017). *International standards and recommended practices (SARPs). Annex 10 to the convention of international civil aviation. Volume I - Radio navigation aids* (tech. rep.).

Kim, D., Yoon, M., Pullen, S., & Lee, J. (2021). Closed-form analysis of undetected range errors due to ionospheric impacts for GBAS category I operations. *NAVIGATION*, *68*(3), 507–519. https://doi.org/10.1002/navi.442

Lee, J., Luo, M., Pullen, S., Park, Y. S., Enge, P., & Brenner, M. (2006). Position-domain geometry screening to maximize LAAS availability in the presence of ionosphere anomalies. *Proceedings of the 19th International Technical Meeting of the Satellite Division of the Institute of Navigation (ION GNSS 2006)*, 393–408. https://www.ion.org/publications/abstract.cfm?articleID=6900

Lee, J., Pullen, S., Datta-Barua, S., & Lee, J. (2016). Real-time ionospheric threat adaptation using a space weather prediction for GNSS-based aircraft landing systems. *IEEE Transactions on Intelligent Transportation Systems*, *18*(7), 1752–1761. https://doi.org/10.1109/TITS.2016.2627600

Lee, J., Seo, J., Park, Y., Pullen, S., & Enge, P. (2011). Ionospheric threat mitigation by geometry screening in ground-based augmentation systems. *Journal of Aircraft*, *48*(4), 1422–1433. https://doi.org/10.2514/1.C031309

Marini-Pereira, L., de Oliveira Moraes, A., & Pullen, S. (2024). A simple and effective approach to real-time ionospheric monitoring at low latitudes and its applicability to GBAS. *NAVIGATION*, *71*(1). https://doi.org/10.33012/navi.619

Mayer, C., Belabbas, B., Jakowski, N., Meurer, M., & Dunkel, W. (2009). Ionosphere threat space model assessment for GBAS. *Proceedings of the 22nd International Technical Meeting of the Satellite Division of the Institute of Navigation (ION GNSS 2009)*, 1091–1099. https://www.ion.org/publications/abstract.cfm?articleID=8518

McGraw, G. A., Murphy, T., Brenner, M., Pullen, S., & Dierendonck, A. J. V. (2000). Development of the LAAS accuracy models. *Proceedings of the 13th International Technical Meeting of the Satellite Division of the Institute of Navigation (ION GPS 2000)*, 1212–1223. https://www.ion.org/publications/abstract.cfm?articleID=1523

Misra, P., & Enge, P. (2006). *Global Positioning System: Signals, measurements and performance* (2nd ed.). Massachusetts: Ganga-Jamuna Press.

Pullen, S., Cassell, R., Johnson, B., Brenner, M., Weed, D., Cypriano, L., Topland, M., Stakkeland, M., Pervan, B., Harris, M., Saito, S., Lee, J., Clark, B., Beauchamp, S., & Dennis, J. (2017). Impact

of ionospheric anomalies on GBAS GAST D service and validation of relevant ICAO SARPs requirements. In *Proceedings of the 30th International Technical Meeting of the Satellite Division of the Institute of Navigation (ION GNSS+ 2017)*, 2085–2105. https://doi.org/10.33012/2017.15135

Pullen, S., & Enge, P. (2007). An overview of GBAS integrity monitoring with a focus on ionospheric spatial anomalies. *Indian Journal of Radion & Space Physics (94.20. Vv; 94.20 B6)*, *36*, 249–260. https://nopr.niscpr.res.in/bitstream/123456789/4705/1/IJRSP%2036(4)%20249-260.pdf

Pullen, S., Park, Y. S., & Enge, P. (2009). Impact and mitigation of ionospheric anomalies on ground-based augmentation of GNSS. *Radio Science*, *44*. https://doi.org/10.1029/2008RS004084

Ramakrishnan, S., Lee, J., Pullen, S., & Enge, P. (2008). Targeted ephemeris decorrelation parameter inflation for improved LAAS availability during severe ionosphere anomalies. In *Proceedings of the 2008 National Technical Meeting of the Institute of Navigation*, 354–366. https://www.ion.org/publications/abstract.cfm?articleID=7694

RTCA. (2017). *DO-253D, Minimum operational performance standards for GPS local area augmentation system airborne equipment* (tech. rep.).

Saito, S., Sunda, S., Lee, J., Pullen, S., Supriadi, S., Yoshihara, T., Terkildsen, M., Lecat, F., & Force, I. A. I. S. T. (2017). Ionospheric delay gradient model for GBAS in the Asia-Pacific region. *GPS Solutions*, *21*(4), 1937–1947. https://doi.org/10.1007/s10291-017-0662-1

Seo, J., Lee, J., Pullen, S., Enge, P., & Close, S. (2012). Targeted parameter inflation within ground-based augmentation systems to minimize anomalous ionospheric impact. *Journal of Aircraft*, *49*(2), 587–599. https://doi.org/10.2514/1.C031601

Shively, C. A., & Niles, R. (2008). Safety concepts for mitigation of ionospheric anomaly errors in GBAS. In *Proceedings of the 2008 National Technical Meeting of the Institute of Navigation*, 367–381. https://www.ion.org/publications/abstract.cfm?articleID=7695

Silva, W. d. C., & Monico, J. F. G. (2022). GBAS: Fundamentals and availability analysis according to σ vig. *Journal of Geodetic Science*, *12*(1), 22–37. https://doi.org/10.1515/jogs-2022-0132

Simili, D. V., & Pervan, B. (2006, April). Code-carrier divergence monitoring for the GPS local area augmentation system. In *Proceedings of the IEEE/ION Position, Location, And Navigation Symposium (PLANS 2006)*, 483–493. https://doi.org/10.1109/PLANS.2006.1650636

U.S. Department of Defense. (2008, September). *Global Positioning System standard positioning service performance standard* (4th ed.).

Yoon, M., Kim, D., & Lee, J. (2020). Extreme ionospheric spatial decorrelation observed during the March 1, 2014, equatorial plasma bubble event. *GPS Solutions*, *24*(2), 1–11. https://doi.org/10.1007/s10291-020-0960-x

Yoon, M., Kim, D., Lee, J., Rungruengwajiake, S., & Pullen, S. (2016). Assessment of equatorial plasma bubble impacts on ground-based augmentation systems in the brazilian region. In *Proceedings of the 2016 International Technical Meeting of the Institute of Navigation*, 368–379. https://doi.org/10.33012/2016.13423

Yoon, M., Kim, D., Pullen, S., & Lee, J. (2019). Assessment and mitigation of equatorial plasma bubble impacts on category I GBAS operations in the Brazilian region. *NAVIGATION, 66*(3), 643–659. https://doi.org/10.1002/navi.328

Yoon, M., Lee, J., & Pullen, S. (2020). Integrity risk evaluation of impact of ionospheric anomalies on GAST D GBAS. *NAVIGATION*, *67*(2), 223–234. https://doi.org/10.1002/navi.339

Yoon, M., Lee, J., Pullen, S., Gillespie, J., Mathur, N., Cole, R., de Souza, J., Doherty, P., & Pradipta, R. (2017). Equatorial plasma bubble threat parameterization to support GBAS operations in the Brazilian region. *NAVIGATION, 64*(3), 309–321. https://doi.org/10.1002/navi.203

How to cite this article: Caamano, M., Juan, J.M., Sanz, J., & Pullen, S. (2026). Real-time ionospheric threat adaptation to increase CAT-I GBAS availability in equatorial regions. *NAVIGATION, 73*. https://doi.org/10.33012/navi.754